Article

Tractable mouse TNBC models capture the heterogeneous tumor immune microenvironment and adaptation to PD-L1 blockade

Check for updates

Robbe Salembier[1,2], Caro De Haes[1,2], Kristel Demeyere[1], Steven Van Laere[3], Lucie Cervenkova[4], Nicolaas Van Renne[4], Christos Sotiriou[4], Evelyne Meyer[1,2,5] & Jonas Steenbrugge[1,2,5] ✉

Triple-negative breast cancer (TNBC) patients exhibit variable responses to programmed death (PD)-ligand (L)1 blockade, largely determined by the 'hot' vs 'cold' state of the tumor immune microenvironment (TIME). We here characterized nine mouse TNBC models, relying on intraductal mammary gland inoculation of established mouse TNBC cell lines, with a heterogeneous TIME to study anti-PD-L1 resistance mechanisms. Complementary in vitro and in vivo screening classified the 4T1-hot-based model, a highly inflamed control through its immunogenic luciferase tag expression compared to the untagged 4T1-cold-based model, as displaying the 'hottest' TIME. However, both 4T1-based counterparts did not respond to anti-PD-L1, which was attributed to their immunosuppressive myeloid cell content, as well as upregulation of cancer-associated fibroblasts in the 4T1-hot and high PD-L1-expressing CXCL10^{+} tumor-associated macrophages in 4T1-cold primary tumors. These anti-PD-L1 adaptation mechanisms across TIME states, as captured by the mouse TNBC models, highlight specific cellular targets for future studies.

The aggressive triple-negative breast cancer (TNBC) subtype is now routinely treated with immune checkpoint blockade (ICB) in combination with chemotherapy[1,2]. ICB employs antibodies targeting immune checkpoints such as programmed death (PD)-1 and PD-ligand (L)1 in the tumor immune microenvironment (TIME), thereby preventing T-cell exhaustion and enhancing tumor cell killing[3]. In patients with early-stage TNBC, ICB has increased pathological complete response (pCR) rates to as high as 60%[4].

A major determinant of ICB efficacy in TNBC is the immunological status of the TIME, often classified as 'cold' or 'hot' based on the degree of lymphocyte infiltration[5,6]. TNBC patients with a 'cold' TIME, characterized by minimal lymphocytic infiltration, are associated with poor prognosis and low responsiveness to immunotherapy[7]. However, even a lymphocyte-rich 'hot' TIME does not necessarily ensure improved ICB outcomes as a result of adaptive resistance mechanisms that remain incompletely understood[8]. To investigate how different TIME states contribute to immune evasion and

ICB resistance, robust preclinical models that recapitulate the heterogeneous immune landscapes of human TNBC are essential[9].

To address this need, the current study comprehensively characterizes nine mouse TNBC models generated by intraductal inoculation of established TNBC cell lines in the mammary gland of syngeneic mouse strains. This orthotopic inoculation method uniquely recapitulates the complete TNBC disease process from ductal carcinoma in situ (DCIS) to invasive carcinoma (IC), within an intact immune system[10]. The cell lines, derived from three different mouse strains (i.e., BALB/C-derived 4T1-hot, 4T1-cold, EMT6, D2A1 and 66CL4 cells, C57BL/6-derived Py230 and AT3 cells, FVB/N-derived MVT1 and MET1 cells), were first analyzed in vitro for differences in growth kinetics and gene expression. Following their intraductal inoculation, TIME heterogeneity was evaluated through primary tumor growth dynamics, spontaneous lung metastasis, transcriptomic profiling, and immune cell composition. Using the ICB-resistant 4T1-cold and 4T1-hot model further identified distinct anti-PD-L1 resistance mechanisms,

[1]Laboratory of Biochemistry, Department of Veterinary and Biosciences, Faculty of Veterinary Medicine, Ghent University, Merelbeke, Belgium. [2]Cancer Research Institute Ghent (CRIG), Ghent, Belgium. [3]Center for Oncological Research (CORE), Faculty of Medicine and Health Sciences, University of Antwerp, Wilrijk, Belgium. [4]Breast Cancer Translational Research Laboratory, Institut Jules Bordet, Hôpital Universitaire de Bruxelles (H.U.B), Université Libre de Bruxelles (ULB), Brussels, Belgium. [5]These authors contributed equally: Evelyne Meyer, Jonas Steenbrugge. ✉e-mail: Jonas.Steenbrugge@ugent.be

BCRF

1

including the upregulation of CXCL10$^+$ tumor-associated macrophages (TAMs) and cancer-associated fibroblasts (CAFs), which may be relevant across TIME states.

Collectively, these mouse TNBC models capture the heterogeneous TNBC TIME and provide a powerful platform for the discovery of therapeutic targets aimed at enhancing ICB efficacy.

Results

In vitro characterization of mouse TNBC cell lines

The 9 selected mouse TNBC cell lines (i.e., 4T1-hot, 4T1-cold, 66CL4, EMT6, D2A1, AT3, PY230, MET1 and MVT1), aimed to develop a heterogeneous 'hot' vs 'cold' TIME as observed in TNBC patients, were first characterized in vitro. An imaging system that allowed evaluation of the kinetic growth of the cell lines based on their speed in occupying space in the culture well identified EMT6 as the fastest-growing cell line (Supplementary Fig. 1a, b). More specifically, the slope of EMT6 cellular growth was significantly higher after 52 h of culturing compared to the eight other cell lines, whereas the 66CL4 cell line displayed the lowest cellular growth slope (Supplementary Fig. 1b). The 4T1-hot cell line also showed a significantly higher slope of growth after 52 h of culturing compared to 7 other cell lines, including its 4T1-cold counterpart (Supplementary Fig. 1b). In contrast to its low slope of cellular growth, the 66CL4 cell line had a significantly higher number of cells after 48 h of growth compared to all other cell lines, highlighting the need to also take this parameter into account when classifying cell lines as slow- or fast-growing (Supplementary Fig. 1c). Based on these combined parameters, PY230 and AT3 could be labeled as the slowest-growing of all 9 cell lines (Supplementary Fig. 1b, c). Subsequent characterization using single-cell RNA-sequencing (scRNA-seq) indicated clear differences between the 9 cell lines at the transcriptomic level based on their distinctly separate uniform manifold approximation and projection (UMAP) clustering (Fig. 1a). Cell lines were identified as triple-negative based on the absence or low expression of *Erbb2*, *Esr2*, and *Pgr* transcripts

(Fig. 1b). Although the EMT6 cell line showed consistently high expression of *Esr1*, a previous study demonstrated that EMT6 cells are not growth-stimulated by estradiol supplementation[11] and hence remain frequently reported as triple-negative[12–15]. The EMT6 cell line also displayed a prominent inflammatory profile with high expression of *Csf1*, *Jak1*, and *Cxcl5* (Fig. 1c, d). Expression of *Mif* and *Spp1*, two targets associated with immunosuppression in cancer patients[16,17], was detected in all cell lines (Fig. 1d). Linking the gene expression profiles of the cell lines to the hallmarks of cancer using GSEA highlighted clear differences in epithelial-to-mesenchymal transition (EMT), growth-supporting metabolism and inflammatory state (Fig. 1e). More specifically, EMT6, PY230 and AT3 displayed significantly increased expression of EMT genes compared to the other cell lines, but both the PY230 and AT3 cell line also showed a significantly decreased expression of MYC target genes associated with cellular mitosis (Fig. 1e). Furthermore, the 4T1-cold, 66CL4 and PY230 cell line showed significantly lower expression of genes associated with either fatty acid metabolism, glycolysis, oxidative phosphorylation or mTORC1 signaling (Fig. 1e)[18]. A significantly increased expression of interferon (IFN)-α and -γ genes in the EMT6 cell line corroborates its inflammatory nature. These hallmarks for inflammation were also significantly increased in the MET1 and D2A1 cell line, but significantly reduced in the PY230 and AT3 cell line compared to the other cell lines (Fig. 1e).

Growth kinetics and metastatic behavior of the mouse TNBC cell line-derived primary tumors

In order to establish immunocompetent and complementary mouse models from the characterized mouse TNBC cell lines, the cells were intraductally (i.e., truly orthotopically) inoculated in the mammary gland of syngeneic mouse strains. The inoculum dose for each cell line was determined based on the ability to transition from DCIS to IC and to develop palpable tumors (20–30 mm^3 size) by 2 weeks (w) post-inoculation (p.i.). Our group already
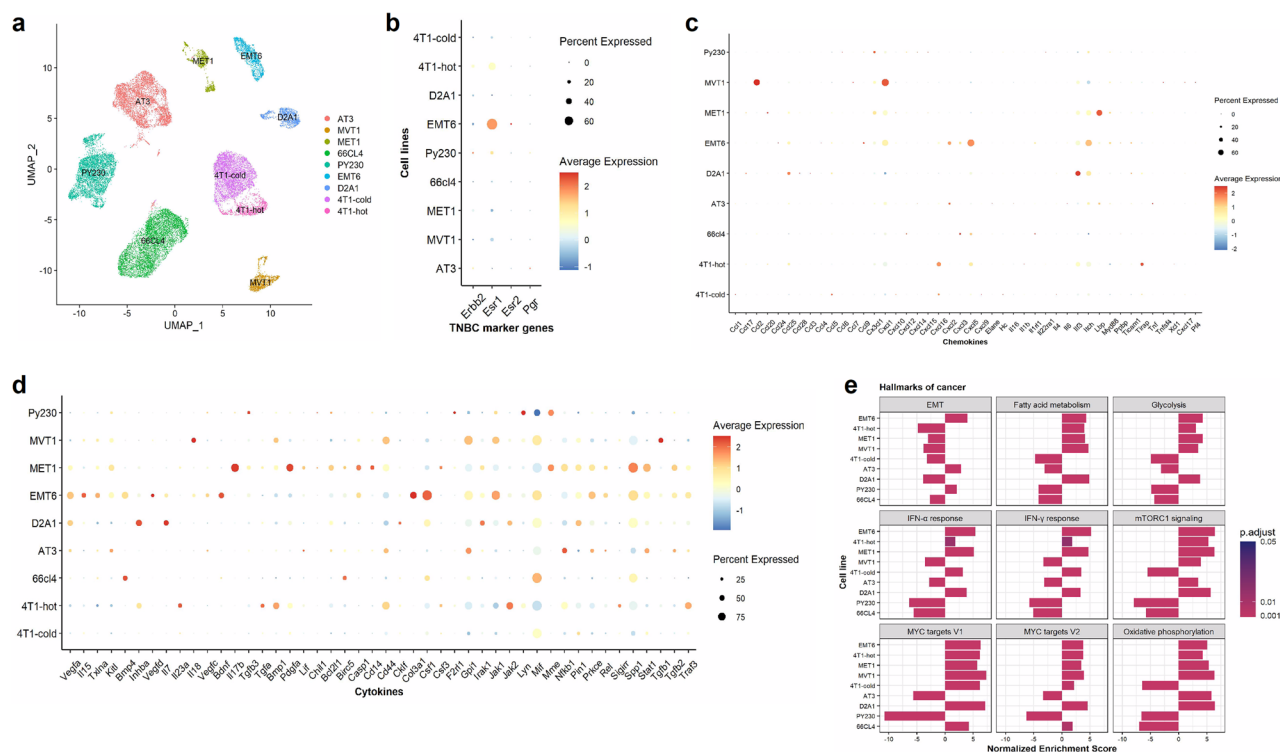

Fig. 1 | In vitro characterization of 9 complementary mouse TNBC cell lines. **a** UMAP plot of the 9 mouse TNBC cell lines. **b** Dot plot showing the average expression and fractions of expressed cells for the 4 clinically relevant marker genes used to diagnose TNBC. **c, d** Dot plots representing the average expression and fractions of expressed cells for each cell line regarding selected chemokines (**c**) and cytokines (**d**). **e** GSEA bar graph showing the normalized enrichment score (NES) of selected significantly expressed cancer hallmarks for each cell line.
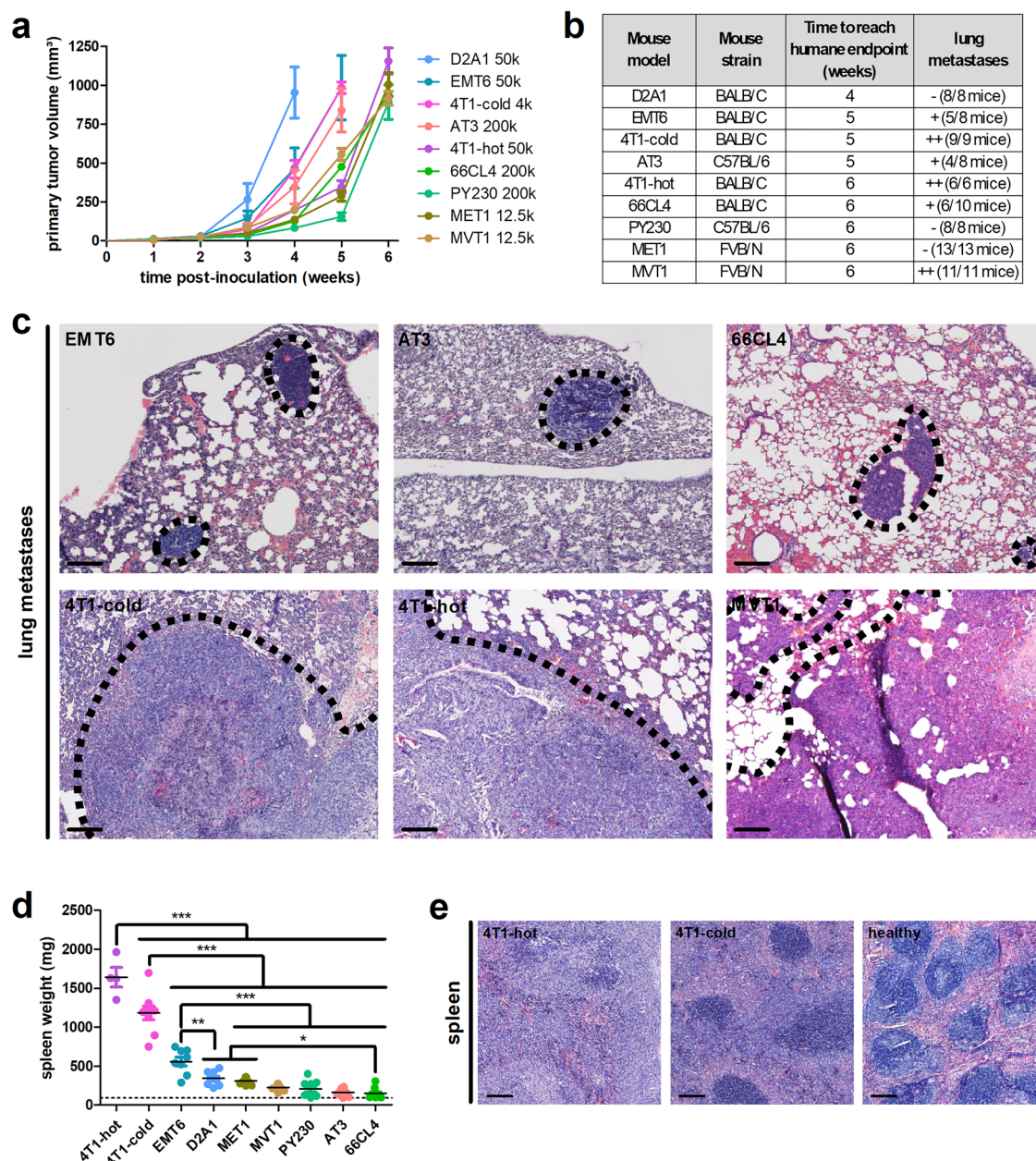
Fig. 2 | Growth kinetics and metastatic behavior of 9 mouse TNBC cell line-derived primary tumors. a Weekly monitoring of primary tumor growth following orthotopic inoculation of mouse TNBC cell lines in syngeneic mouse mammary glands. **b** Lung metastases when primary tumors reached their humane endpoint (i.e., 1 cm³ size). **c** H&E histology of lung metastases in the EMT6-, AT3-, 66CL4-, 4T1-cold-, 4T1-hot- and MVT1-based model. Scale bars = 200 μm. **d** Weight of the spleen isolated from the mouse TNBC models when primary tumors reached their humane endpoint. The dotted line highlights the mean spleen weight of 4 healthy mice. **e** H&E histology of the spleen derived from the 4T1-hot- and 4T1-cold-based model, with histology of a healthy spleen for comparison. Scale bars = 200 μm. Data in **a, d** are presented as the means ± standard error of the mean (SEM). $^*p < 0.05$, $^{**}p < 0.01$, $^{***}p < 0.001$.

identified the optimal inoculum dose of 4T1-hot and 66CL4 cells needed for such a timely DCIS-to-IC transition and efficient metastasis[19]. Characterizing a similar optimal dose for the 7 other cell line-based models subsequently allowed comparison of their growth kinetics and metastatic behavior after the 2 w.p.i. timepoint. More specifically, D2A1 primary tumors showed the fastest growth and reached their humane endpoint (i.e., 1 cm³ primary tumor size) in only 4 weeks (Fig. 2a, b). EMT6, 4T1-cold and AT3 primary tumors also showed rapid growth, reaching their humane endpoint at 5 w.p.i. (Fig. 2a,b). Notably, a low dose of 4×10^3 4T1-cold cells was sufficient for proficient primary tumor growth. In contrast, 4T1-hot, 66CL4, PY230, MVT1 and MET1 required a higher cell dose to eventually develop primary tumors that reached the humane endpoint at 6 w.p.i. (Fig. 2a, b). Metastatic capacity for each primary tumor was scored based on

hematoxylin & eosin (H&E) histology of lung metastases at their respective humane endpoints. More specifically, lung metastases were detected in 6 models: EMT6, AT3, 66CL4, 4T1-cold, 4T1-hot and MVT1. The EMT6-, AT3- and 66CL4-based model showed microscopic-sized lung metastases in only some of the mice at humane endpoint and were therefore scored as '+'/'weakly metastatic'. The 4T1-cold-, 4T1-hot- and MVT1-based model showed macroscopic-sized lung metastases in all mice at humane endpoint and were therefore scored as '++'/'highly metastatic' (Fig. 2b, c). As previously described, the metastatic behavior and associated leukocyte reactions in 4T1-based mouse models can also be determined through enlargement of the spleen and increased spleen weight[20,21]. Both the 4T1-cold- and 4T1-hot-based models showed prominent splenomegaly compared to the other models, with spleen weight in the 4T1-hot-based model

being significantly higher than in the 4T1-cold-based model (Fig. 2d). This was also reflected by a more disturbed splenic architecture and additional loss of white pulp areas on H&E histology (Fig. 2e).

Transcriptomic profiling of the cell line-derived primary tumors at an early timepoint

In order to investigate in depth the TIME differences between the 9 mouse TNBC models, we investigated and compared their primary tumors both at an early timepoint (i.e., at 2 w.p.i., when primary tumors have a similar size of 20–30 mm³) and late timepoint (i.e., at humane endpoint, when primary tumors have a similar size of 1 cm³) (Fig. 3a). On the early timepoint samples, we aimed to apply bulk RNA-sequencing for transcriptomic profiling due to the small amount of available primary tumor tissue (Fig. 3a). On the late timepoint samples, we aimed to perform flow cytometric immunophenotyping with complementary cytokine and immune checkpoint profiling, as well as immunohistochemical analysis for a more thorough immune cell characterization (Fig. 3a).

Following isolation at the early (2 w.p.i.) timepoint, transition from the DCIS to IC stage was first verified in all primary tumors with cytokeratin 5 staining, showing disruption of the ductal myoepithelial barrier by the tumor cells and their breakthrough into the mammary fat pad (Supplementary Fig. 2a). Bulk RNA-seq data of primary tumors were subsequently processed to obtain differentially expressed genes (DEGs) compared to the respective healthy mammary gland transcriptome, excluding the mouse strain-dependent differences and potential transcripts of healthy mammary gland tissue. The DEGs were ranked based on their log2-fold change in expression relative to the healthy gland state and categorized into hallmarks of cancer using GSEA (Fig. 3b). The primary tumors displayed similarity in metabolic hallmarks, with a significant upregulation of glycolysis-based metabolism and downregulation of oxidative phosphorylation and fatty acid metabolism (Fig. 3b). The EMT hallmark was significantly downregulated in PY230 and 66CL4 primary tumors, and non-significantly in AT3 primary tumors (Fig. 3b), whereas MYC target genes, as well as other cellular mitosis hallmarks such as E2F targets, G2M checkpoint, mitotic spindle and mTORC1 signaling were consistently upregulated in all primary tumors (Fig. 3b and Supplementary Fig. 3). Gene expression related to inflammation, as captured by the IFN-α and -γ response, inflammatory response, allograft rejection, IL-6/JAK/STAT3 signaling and TNF-α signaling via NF-κB hallmarks, was significantly downregulated in AT3 primary tumors and non-significantly in D2A1 primary tumors (Fig. 3b and Supplementary Fig. 3). These results suggest a 'cold'/immune cell-deprived TIME state for the AT3 and D2A1 primary tumors, and were corroborated by heatmaps showing reduced expression of gene signatures related to IFN-α and -γ signaling, T-cell activation, T-cell exhaustion, TAMs, antigen presentation and tumor-associated neutrophils (TANs) in both these primary tumors (Fig. 3c and Supplementary Fig. 2b–f). Corroborating their presumed association with a 'hot' TIME, 4T1-hot primary tumors showed an increased pro-inflammatory and T-cell-related gene expression compared to 4T1-cold primary tumors (Fig. 3d). The 4T1-hot TIME identity was also reflected by increased expression of gene signatures related to T-cell activation, T-cell exhaustion and antigen presentation compared to their 4T1-cold counterparts (Fig. 3e). Heterogeneity between the mouse TNBC models was further demonstrated based on gene signatures from recently identified TIME landscapes[22] (Supplementary Fig. 2g, h). More specifically, the highly inflamed TIME of 4T1-hot primary tumors was concomitantly categorized as fully immunomodulatory (IM), whereas the 66CL4, EMT6 and even 4T1-cold TIME was categorized as 70% IM and 30% mesenchymal stem-like (MSL) with fibrovascular structures (Supplementary Fig. 2h). The cold and immune-deprived TIME of D2A1 and AT3 primary tumors was categorized as fully and 75% mesenchymal (M), respectively (Supplementary Fig. 2h). The AT3 TIME also displayed a 25% basal-like (BL) phenotype, characterized by high proliferation (Supplementary Fig. 2h). The MET1 primary tumors were even more proliferative based on their 70% BL annotation and were the only ones to display 30% luminal androgen receptor (LAR) TIME characteristics (Supplementary Fig. 2h). The MVT1

TIME was specified as fully MSL, whereas the PY230 TIME was characterized as the most heterogeneous of all models with 50% MSL-, 25% IM-, 25% BL- and also upregulation of LAR-associated gene expression (Supplementary Fig. 2g, h).

Immunophenotyping of the cell line-derived primary tumors at a late timepoint

Immunophenotyping of primary tumors at a late (1 cm³ size) timepoint enabled evaluation of TIME heterogeneity at the cellular level between the mouse TNBC models. PD-L1 expression was significantly higher in the 4T1-hot primary tumors compared to the 4T1-cold primary tumors based on flow cytometry and compared to all primary tumors based on Luminex assay (Fig. 4a and Supplementary Fig. 4a). We decided to further focus on the 4T1 counterparts with a 'hot' vs 'cold' TIME on an identical strain background, and attributed their differential PD-L1 levels to a significantly higher PD-L1 expression on the tumor cells and not the immune cells (Fig. 4b, c). Strikingly, the numbers of CD45⁺ leukocytes did not significantly differ between the 4T1-cold and 4T1-hot primary tumors (Fig. 4d). When comparing 4T1-cold and 4T1-hot primary tumors with all other models, CD45⁺ leukocyte numbers were significantly higher than in the PY230 and AT3 primary tumors, similar to those in EMT6 and D2A1 primary tumors and significantly lower than in the 66CL4 primary tumors (Supplementary Fig. 4b). Moreover, polymorphonuclear (PMN)-myeloid-derived suppressor cell (MDSC) and monocytic (M)-MDSC numbers were significantly higher in the 4T1-hot and 4T1-cold primary tumors compared to all other primary tumors (Supplementary Fig. 4c, d). This finding was corroborated by significantly higher levels of the PMN-MDSC- and TAN-supporting cytokine granulocyte-colony stimulating factor (G-CSF) in 4T1-cold and 4T1-hot primary tumor lysates (Supplementary Fig. 4e). Yet, despite similar PMN-MDSC numbers in both primary tumors, the 4T1-cold primary tumors displayed even higher levels of G-CSF than their 4T1-hot counterparts (Supplementary Fig. 4e). In contrast to PMN-MDSCs as TAN precursors, the numbers of mature TANs were significantly higher in EMT6 primary tumors compared to all other primary tumors, with the exception of the 4T1-cold and 4T1-hot primary tumors (Supplementary Fig. 4f). This TAN-rich TIME was also corroborated by significantly higher macrophage inflammatory protein (MIP)-2 levels in EMT6 primary tumor lysates (Supplementary Fig. 4 g). Furthermore, the numbers of mature TAMs were significantly higher in 66CL4 primary tumors compared to all other primary tumors (Supplementary Fig. 4h). In line with their 'hot' TIME, a significantly higher abundance of anti-tumorigenic M1- compared to pro-tumorigenic M2-polarized TAMs, as demonstrated by the high M1/M2 TAM ratio, was detected in 4T1-hot compared to 4T1-cold and all other primary tumors (Fig. 4e and Supplementary Fig. 4i).

DC, CD4⁺, and CD8α⁺ T-cell numbers were significantly increased in 4T1-hot primary tumors compared to the 4T1-cold and most other primary tumors (Fig. 4f–h and Supplementary Figs. 4j, and 5a, b). The 66CL4 primary tumors showed a similar number of CD4⁺ and CD8α⁺ T-cells compared to the 4T1-hot primary tumors (Supplementary Fig. 5a, b). The 4T1-hot primary tumors additionally showed strong T-cell activation, based on a high positivity for granzyme B, PD-1 and IFN-γ in the CD8α⁺ T-cell population (Fig. 4i and Supplementary Fig. 5c–e), with the latter being significantly higher than in the 4T1-cold and all other primary tumors, and also reflected by significantly higher IFN-γ levels in 4T1-hot primary tumor lysates (Supplementary Fig. 5f). A similarly high granzyme B positivity in the AT3 and 4T1-cold primary tumors as in the 4T1-hot model indicated that the few CD8α⁺ T-cells present in their 'cold' TIME are activated (Supplementary Fig. 5c). Ki67 positivity of CD8α⁺ T-cells was not significantly different between all primary tumors, highlighting that CD8α⁺ T-cell proliferation is not influenced by the TIME state (Supplementary Fig. 5g). Significantly higher numbers of immunosuppressive FoxP3⁺ CD4⁺ T-regs in the 4T1-cold primary tumors compared to the 4T1-hot and other primary tumors corroborated their immunosuppressed TIME state (Fig. 4j and Supplementary Fig. 5h). B-cell and natural killer (NK)-T cell numbers did not significantly differ between the primary tumors (Supplementary Fig. 5i, j).
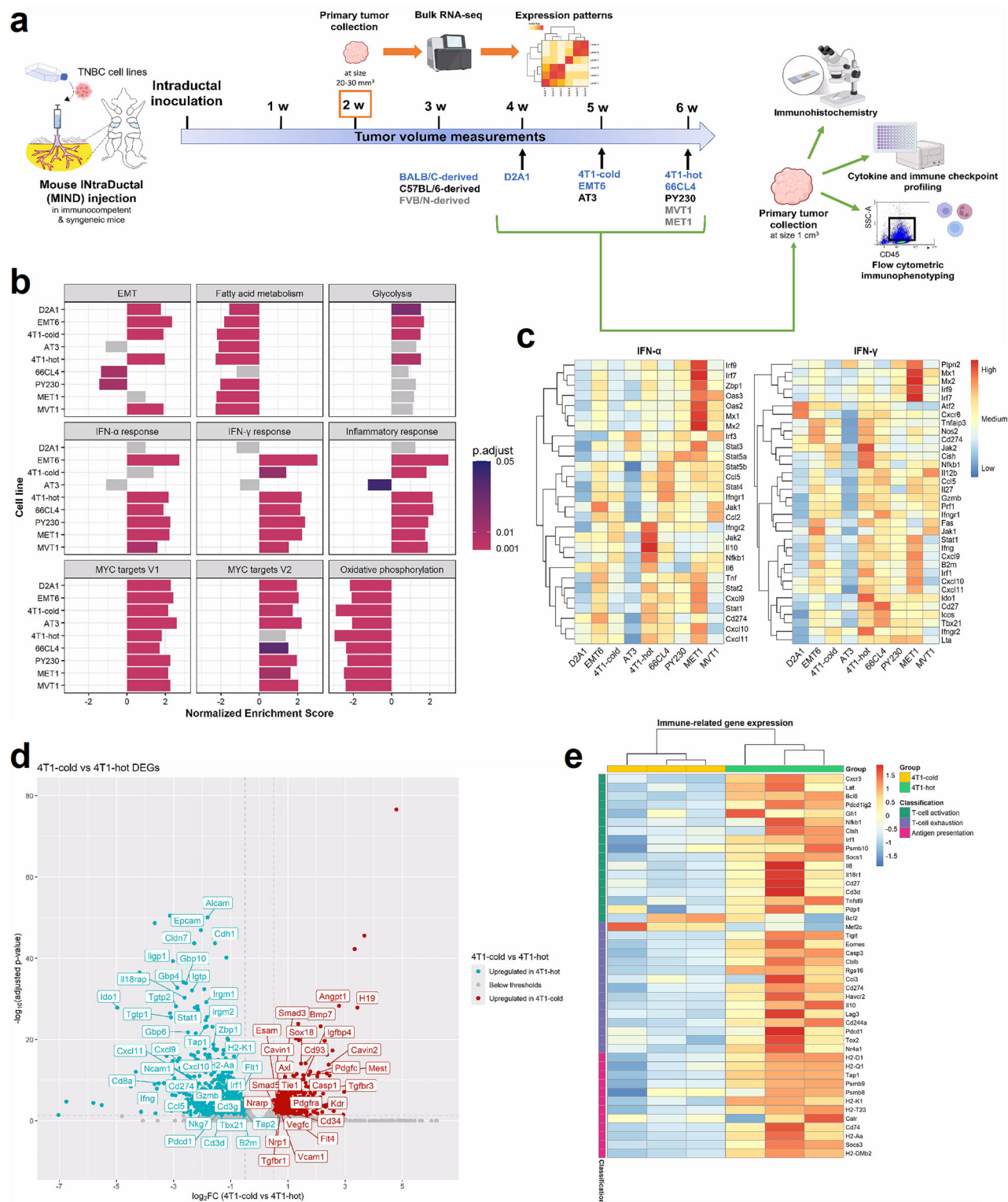
Fig. 3 | Transcriptomic heterogeneity between 9 mouse TNBC cell line-derived primary tumors at an early timepoint. a Experimental timeline showing primary tumor collection and performed techniques at both early timepoints (at primary tumor size of 20–30 mm³) and late timepoints (at primary tumor size of 1 cm³) for all mouse TNBC cell line-based models. **b** GSEA bar graph showing the NES of selected cancer hallmarks for each primary tumor compared to healthy mammary glands. **c** Heatmaps showing row-normalized expression across primary tumors compared to healthy mammary glands for genes associated with IFN-α and IFN-γ signaling. **d** Volcano plot showing differential gene expression in 4T1-hot (left) and 4T1-cold primary tumors (right) with significantly upregulated TIME-related genes labeled (based on adjusted *p*-value); thresholds of the volcano plot were set at adjusted *p*-value = 0.05 and log2-fold change = 0.5. **e** Heatmap showing row-normalized expression in 4T1-cold and 4T1-hot primary tumors for genes associated with T-cell activation, T-cell exhaustion, and antigen presentation.
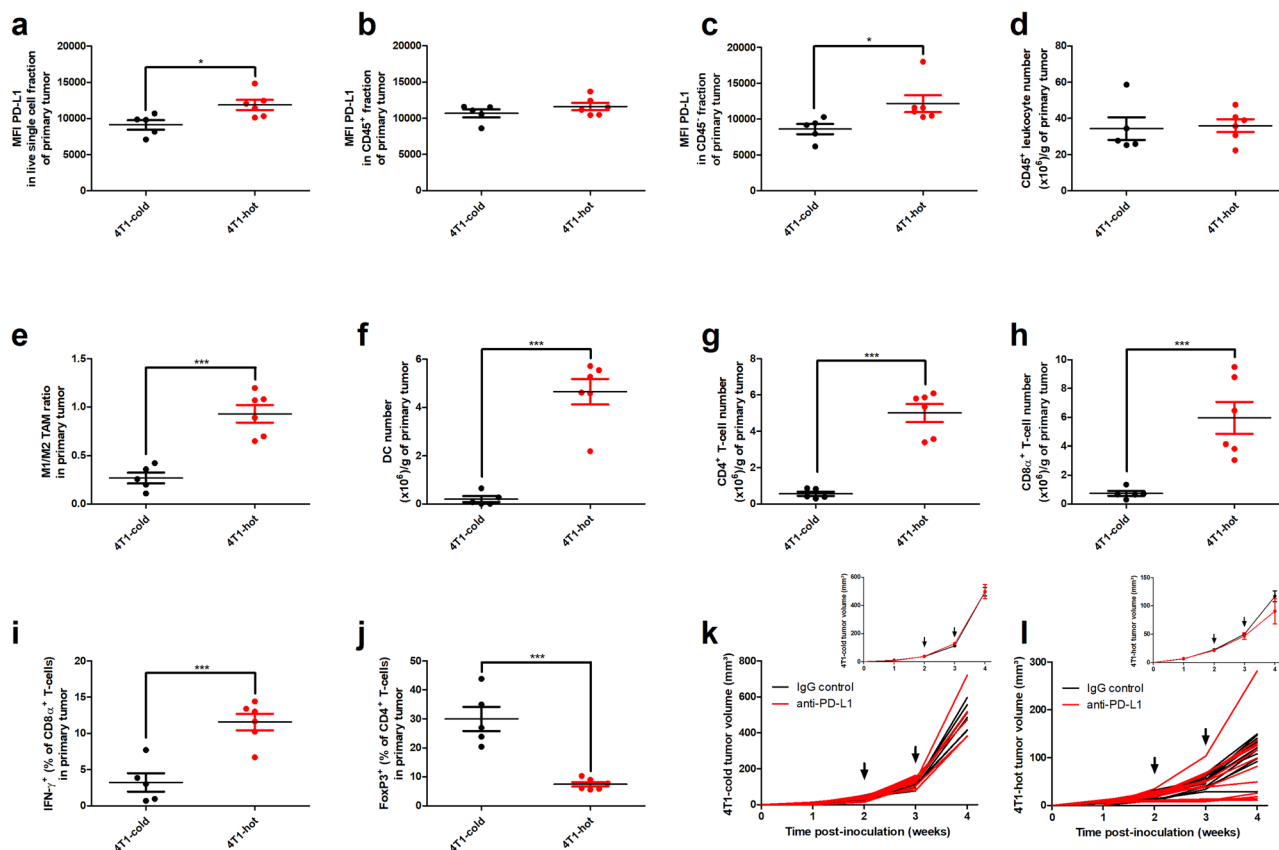
Fig. 4 | Flow cytometric immunophenotyping of 4T1-cold and 4T1-hot primary tumors at a late timepoint. The 4T1-cold and 4T1-hot primary tumors were isolated when reaching 1 cm³ size (i.e., at 5 and 6 w.p.i.) and processed into single cell suspensions for flow cytometric immunophenotyping ($n = 5$ for 4T1-cold and $n = 6$ for 4T1-hot, combined data from 2 experiments are shown). **a–c** PD-L1 expression based on mean fluorescence intensity (MFI) within live single cells (**a**), the CD45$^+$ (**b**), and the CD45$^-$ cell population (**c**). **d** Number of CD45$^+$ leukocytes per gram of primary tumor. **e** Calculated M1/M2 TAM ratio. **f–h** Number of DCs (**f**), CD4$^+$ T-cells (**g**), and CD8α$^+$ T-cells (**h**) per gram of primary tumor. **i** Percentage of IFN-γ$^+$ cells within the CD8α$^+$ T-cell population of primary tumors. **j** Percentage of FoxP3$^+$ cells within the CD4$^+$ T-cell population of primary tumors. **k, l** Weekly measurements of primary tumor volumes in the anti-PD-L1- and IgG control-treated 4T1-cold- (**k**) and 4T1-hot-based model (**l**) ($n = 12$ for both treatment groups across all timepoints in the 4T1-cold-based model, except at 4 w.p.i., where $n = 6$ for both treatment groups; $n = 18$ for both treatment groups across all timepoints in the 4T1-hot-based model, except at 4 w.p.i., where $n = 12$ for both treatment groups). Arrows indicate when anti-PD-L1 or IgG control treatment was administered. Data are presented as the means ± SEM. $^*p < 0.05$, $^{**}p < 0.01$, $^{***}p < 0.001$.

The 66CL4 primary tumors showed significantly higher numbers of NK cells compared to 5 other primary tumors (Supplementary Fig. 5k).

To validate the flow cytometric immunophenotyping and determine the location of major immune cell subtypes, immunohistochemical staining was performed on the primary tumor tissue. The 4T1-cold, 4T1-hot, EMT6 and, to a lesser extent, 66CL4 primary tumors mainly showed accumulation of TANs in necrotic areas, which were identified based on Ly6G positivity (Supplementary Fig. 6a). As also demonstrated through flow cytometry, EMT6 primary tumors showed significantly higher infiltration of Ly6G$^+$ TANs compared to the other primary tumors (Supplementary Fig. 6a). Immunohistochemistry for CD163 verified excessive M2 TAM infiltration, often with spindle-shaped morphology, in the 66CL4 primary tumor core and significantly higher compared to the other primary tumors (Supplementary Fig. 6b). Immunohistochemistry for CD8α corroborated the significantly higher CD8α$^+$ T-cell infiltration, the primary parameter for 'hot' TIME classification, in 4T1-hot primary tumors, scattered throughout the tumor core (Supplementary Fig. 6c).

Transcriptomic adaptation of selected 4T1-cold and 4T1-hot primary tumors to anti-PD-L1 treatment

To evaluate potential differences in anti-PD-L1 efficacy between the 4T1-cold- and 4T1-hot-based model as preclinical reference models containing, respectively, a 'cold' and 'hot' TIME, an additional experiment was set up in which both models received a weekly systemic administration of anti-PD-L1 treatment between 2 and 4 w.p.i. (Fig. 4k, l). However, this treatment strategy did not significantly reduce primary tumor growth compared to IgG isotype control treatment in either model (Fig. 4k, l). In line with previous reports[23,24], the use of murinized anti-PD-L1 instead of the commonly reported rat-derived anti-PD-L1 antibodies was necessary to avoid adverse xenogeneic hypersensitivity reactions in the 4T1-based models.

Despite the absence of tumor growth reduction, at 3 w.p.i. (i.e., after the first dose of anti-PD-L1), 4T1-cold primary tumors showed a significant upregulation of hallmarks related to tumor inflammation (i.e., inflammatory response, IFN-γ and -α response) and significant downregulation of hallmarks related to cellular mitosis and tumor progression (i.e., myogenesis, MYC targets V1 and V2, mitotic spindle, hedgehog signaling, G2M checkpoint, EMT and angiogenesis) (Fig. 5a). In contrast, anti-PD-L1 treatment significantly upregulated the hallmarks related to tumor progression in the 4T1-hot primary tumors, with the exception of the MYC targets V1 and V2 hallmarks, which were similarly downregulated as in the 4T1-cold counterparts (Fig. 5a). Evaluating the 30 most significantly DEGs between IgG control- and anti-PD-L1-treated primary tumors based on adjusted p-value further highlighted the differential adaptation to anti-PD-L1 treatment of the 4T1-based models. More specifically, pro-inflammatory/IFN-stimulated genes *Bst2*, *Cd274*, *Cxcl11*, *Gvin-ps2*, *Icam1*, *Serpina3f* and *Slfn1*, antigen-presenting genes *B2m*, *Cd83*, *Fcgr4*, *H2-Bl*, *H2-DMb1* and *H2-L*, and the anti-angiogenic gene *Chga* were among the most significantly upregulated DEGs associated with anti-PD-L1 treatment in the 4T1-cold primary tumors (Fig. 5b). The most significantly upregulated DEGs in the 4T1-hot primary tumors upon anti-PD-L1 treatment included
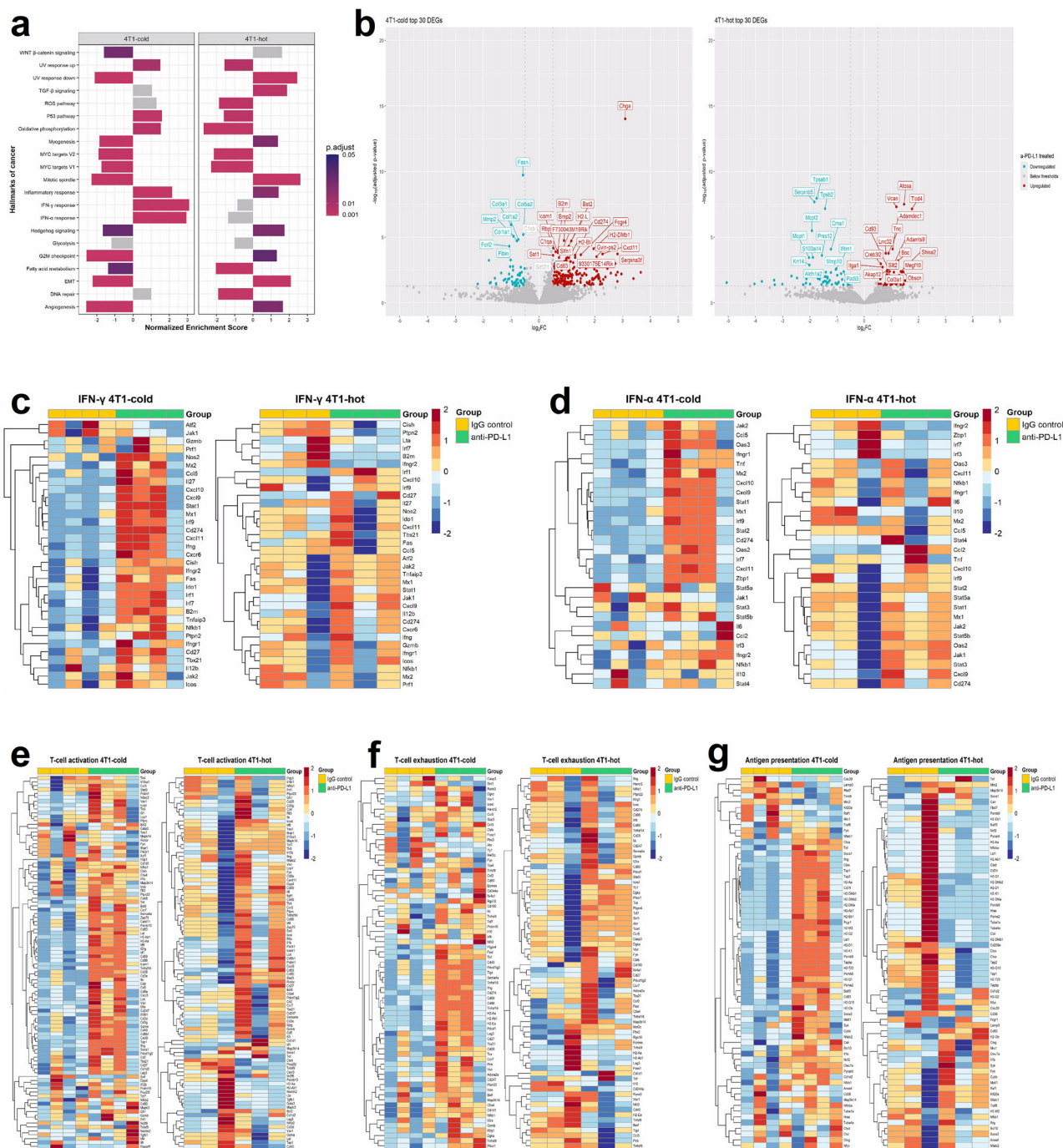
Fig. 5 | Transcriptomic adaptation of 4T1-cold and 4T1-hot primary tumors upon anti-PD-L1 treatment. a GSEA bar graph showing the NES of selected cancer hallmarks based on gene expression changes in both 4T1-cold and 4T1-hot primary tumors upon anti-PD-L1 vs IgG control treatment. **b** Volcano plots showing differential gene expression in anti-PD-L1- vs IgG control-treated 4T1-cold (left) and 4T1-hot primary tumors (right) with the 30 most significant DEGs labeled (based on adjusted *p*-value); thresholds of the volcano plots were set at adjusted *p*-value = 0.05 and log2-fold change = 0.5. **c–g** Heatmaps showing row-normalized expression levels of genes associated with IFN-γ (**c**) and IFN-α signaling (**d**), T-cell activation (**e**), T-cell exhaustion (**f**) and antigen presentation (**g**) in anti-PD-L1- and IgG control-treated 4T1-cold (left) and 4T1-hot primary tumors (right).

extracellular matrix (ECM) and CAF factors (*Adamdec1*, *Adamts9*, *Boc*, *Col3a1*, *Slit2*, *Tnc* and *Vcan*), whereas several related factors (including *Col1a1*, *Col1a2*, *Col3a1*, *Col5a2*, *Fibin* and *Mmp2*) were most significantly downregulated in the 4T1-cold counterparts (Fig. 5b). The most significantly downregulated DEGs in the 4T1-hot primary tumors in response to anti-PD-L1 treatment could be attributed to mast cells (*Cma1*, *Mcpt1*, *Mcpt2*, *Tpsab1* and *Tpsb2*) (Fig. 5b).

In line with pro-inflammatory stimulation, gene signatures associated with IFN-γ and -α, T-cell activation and exhaustion, antigen presentation and

general inflammation were also upregulated in anti-PD-L1- compared to IgG control-treated 4T1-cold primary tumors (Fig. 5c–g and Supplementary Fig. 7a). The 4T1-hot primary tumors were already intrinsically associated with high IFN signaling and showed no additional upregulation of IFN-γ or -α gene signatures upon treatment with anti-PD-L1 compared to IgG control (Fig. 5c, d). T-cell activation-, T-cell exhaustion-, antigen presentation- and general inflammation-associated gene signatures were also not clearly upregulated upon anti-PD-L1 treatment as observed in the 4T1-cold counterparts (Fig. 5e–g and Supplementary Fig. 7a). However, both 4T1-cold and 4T1-hot

primary tumors showed similar expression of TAN-associated genes, including *Chi3l1*, when treated with anti-PD-L1 or IgG control, indicating that the abundant immunosuppressive TAN content in both 4T1-based models remains unaffected by ICB (Supplementary Fig. 7b–d).

Associating anti-PD-L1 adaptation in the 4T1-cold vs 4T1-hot TIME to upregulation of CXCL10+ TAMs and CAFs

In order to associate anti-PD-L1 adaptation in both 4T1-cold and 4T1-hot primary tumors with specific cell subtypes, the significant DEGs identified upon anti-PD-L1 vs IgG control treatment were mapped to a publicly available scRNA-seq dataset from TNBC patient tumors (Fig. 6a)[25]. The significantly upregulated DEGs from 4T1-cold and 4T1-hot primary tumors were strongly represented in the myeloid and CAF cluster of the dataset, respectively (Fig. 6b, c). Further subdivision of these clusters into cellular subtypes allowed annotation of the 4T1-cold- and 4T1-hot-derived upregulated DEGs to CXCL10+ TAMs and myofibroblast-like (my)CAF/inflammatory (i)CAF populations, respectively (Fig. 6d, e). The significantly upregulated DEG list from 4T1-cold primary tumors was subsequently used to establish a 12-gene signature specifically annotated to CXCL10+ TAMs (Supplementary Fig. 8a). The expression of this signature, indicating the presence of the CXCL10+ TAM subset, was also high in the 4T1-hot primary tumors, even upon IgG control treatment, and PD-L1 blockade did not further increase its expression (Fig. 6 f). Evaluation of the CXCL10+ TAM signature in the other characterized mouse TNBC models using the bulk RNA-seq data generated at an early timepoint (i.e., 2 w.p.i.) revealed its high expression in the majority of primary tumors, including EMT6, 66CL4, PY230 and MET1 (Fig. 6 g). The significantly upregulated DEG list from 4T1-hot primary tumors was likewise used to establish a 9-gene signature specifically annotated to myCAF/iCAF (Supplementary Fig. 8b). The expression of this signature was particularly high in the MVT1 and EMT6 primary tumors already at an early timepoint (Fig. 6h). Using publicly available datasets, the CAF signature was associated with significantly decreased distant metastasis-free survival (DMFS) in TNBC patients, as well as significantly decreased progression-free survival (PFS) upon anti-PD-L1 treatment in other cancer types, including bladder cancer and esophageal adenocarcinoma (Supplementary Fig. 8c–e). Mapping the significantly downregulated DEGs from 4T1-cold and 4T1-hot primary tumors to the scRNA-seq dataset further revealed strong representation in the CAF and normal epithelial cluster, respectively (Supplementary Fig. 9a, b). The downregulated DEGs from 4T1-cold primary tumors were more specifically annotated to myCAFs/iCAFs (Supplementary Fig. 9c), whereas those from the 4T1-hot primary tumors were annotated to myoepithelial cells (Supplementary Fig. 9d).

To increase the clinical relevance of the current study, the identified anti-PD-L1 adaptation mechanisms in mouse TNBC models were verified in an RNA-seq dataset of anti-PD-L1-treated human TNBC patients. More specifically, we consulted bulk RNA-seq data from the GeparNuevo trial, in which early-stage TNBC patients uniquely received a single neoadjuvant dose of Durvalumab without chemotherapy, and samples were collected at baseline and 2 weeks after Durvalumab treatment[26]. This trial has a highly similar setup to the mouse TNBC model experiments and contained data of sufficient quality from patients who showed a non-significant increase in pCR rate. The significant DEGs identified in Durvalumab-treated vs baseline primary breast carcinoma were again mapped to a publicly available scRNA-seq dataset from TNBC patient tumors for annotation to distinct cell types in the TIME[25]. Similar to anti-PD-L1 adaptation in the 4T1-cold primary tumors, the significantly upregulated DEGs in the Durvalumab arm were strongly represented in the myeloid cluster of the dataset (Supplementary Fig. 10a) and further subclustering specified their annotation to CXCL10+ TAMs (Supplementary Fig. 10b). Moreover, also similar to anti-PD-L1 adaptation in the 4T1-hot primary tumors, myCAF/iCAF populations were increased based on the upregulated DEGs, and were equally abundant as (exhausted) T-cell populations in the TIME (Supplementary Fig. 10b). The significantly downregulated DEGs in the Durvalumab arm were represented in the epithelial cell clusters (Supplementary Fig. 10c), and

more specifically in myoepithelial and luminal cells, as well as cycling cancer cells (Supplementary Fig. 10d).

Discussion

Our study aimed to characterize 9 cell line-based mouse TNBC models with a focus on their TIME and ICB adaptation mechanisms associated with the 'hot' vs 'cold' TIME state. The mouse TNBC cell lines were first compared in vitro and displayed substantial heterogeneity based on their differential cellular growth and single-cell transcriptomic profiles. In marked contrast to the PY230 and AT3 cell lines, the EMT6 cell line displayed rapid cell growth, corroborated by a high expression of metabolic hallmarks and cyto-/chemokines, as previously described [27]. Whereas the 66CL4 cell line showed the highest number of cells after 48 h growth in culture, their densely packed morphology allowed them to take up minimal space in culture wells with low metabolic activity, resulting in a low slope of cellular growth as identified through live cell imaging. This quiescent character of the 66CL4 cell line was also accompanied by low expression of cyto-/chemokines and hallmarks of inflammation, verifying previous reports[28,29]. The scRNA-seq atlas adds to already-existing single-cell atlases of human breast cancer cell lines[30,31]. Moreover, although derived from the 4T1-cold cell line, the 4T1-hot cells used in our study formed a distinct cellular cluster, and showed intrinsic differences beyond the introduction of luciferase compared to the 4T1-cold cells. These include modestly elevated Esr1 expression, altered cytokine/chemokine profiles, and metabolic hallmarks (such as fatty acid metabolism, glycolysis, and mTORC1 signaling) that may contribute to phenotypic differences. These inherent disparities are a limitation of our study and should be taken into account when interpreting comparisons between the 4T1-hot- and 4T1-cold-based models.

The growth kinetics of the cell lines upon their intraductal inoculation in vivo vastly differed from the in vitro situation, strongly indicating the influence of the TIME on primary tumor progression. D2A1 primary tumors displayed the fastest progression, but did not spontaneously develop lung metastases. PY230 primary tumors showed the slowest progression and were able to catch up in volume with other primary tumors by 6 w.p.i., but also did not spontaneously develop lung metastases, as previously published by our group[32]. In contrast to their in vitro growth, 4T1-cold primary tumors grew faster than their 4T1-hot counterparts, even with a lower number of intraductally inoculated cells, and similarly developed excessive lung metastases. These primary tumor growth and metastatic differences were not caused by a differential cellular metabolism, as all primary tumors similarly switched to glycolysis, concomitantly downregulating their oxidative phosphorylation and fatty acid metabolism already at 2 w.p.i. This glycolytic switch, known as the Warburg effect, involves increased glucose uptake and oxygen-independent reduction of pyruvate to lactate under hypoxic conditions, promoting tumorigenesis[33]. All primary tumors also showed a similar upregulation of the hallmarks MYC targets V1 and V2, highlighting the role of MYC as a major driver of (mammary) tumor progression and immune evasion[34].

The differential inflammatory state of the TIME provided a potential lead to explain the observed heterogeneity between the mouse TNBC models. More specifically, based on immune-related gene signatures and hallmarks of inflammation, D2A1 and AT3 primary tumors were associated with the most prominent 'cold' TIME of all mouse TNBC models, providing a stimulatory basis for primary tumor outgrowth. Similarly, PY230 primary tumors showed poor leukocyte responses, although this may rather be attributed to their progenitor cell state compared to all other primary tumors[35]. Yet, accumulation of immunosuppressive cell types, including TANs, M2 TAMs, PMN- and M-MDSC precursors, and systemic neutrophilia, as displayed by the G-CSF-overexpressing 4T1-based models, are key for primary tumors to efficiently metastasize and fully colonize the lungs. Indeed, it has been shown that mediating G-CSF overexpression in D2A1 and AT3 cells through lentiviral vector transduction or treating EMT6 and 66CL4 primary tumor-bearing mice with recombinant mouse G-CSF significantly increased their lung metastatic efficiency[36–39]. As an exception, MVT1 primary tumors metastasize to the lungs very efficiently without the need for enhanced leukocyte
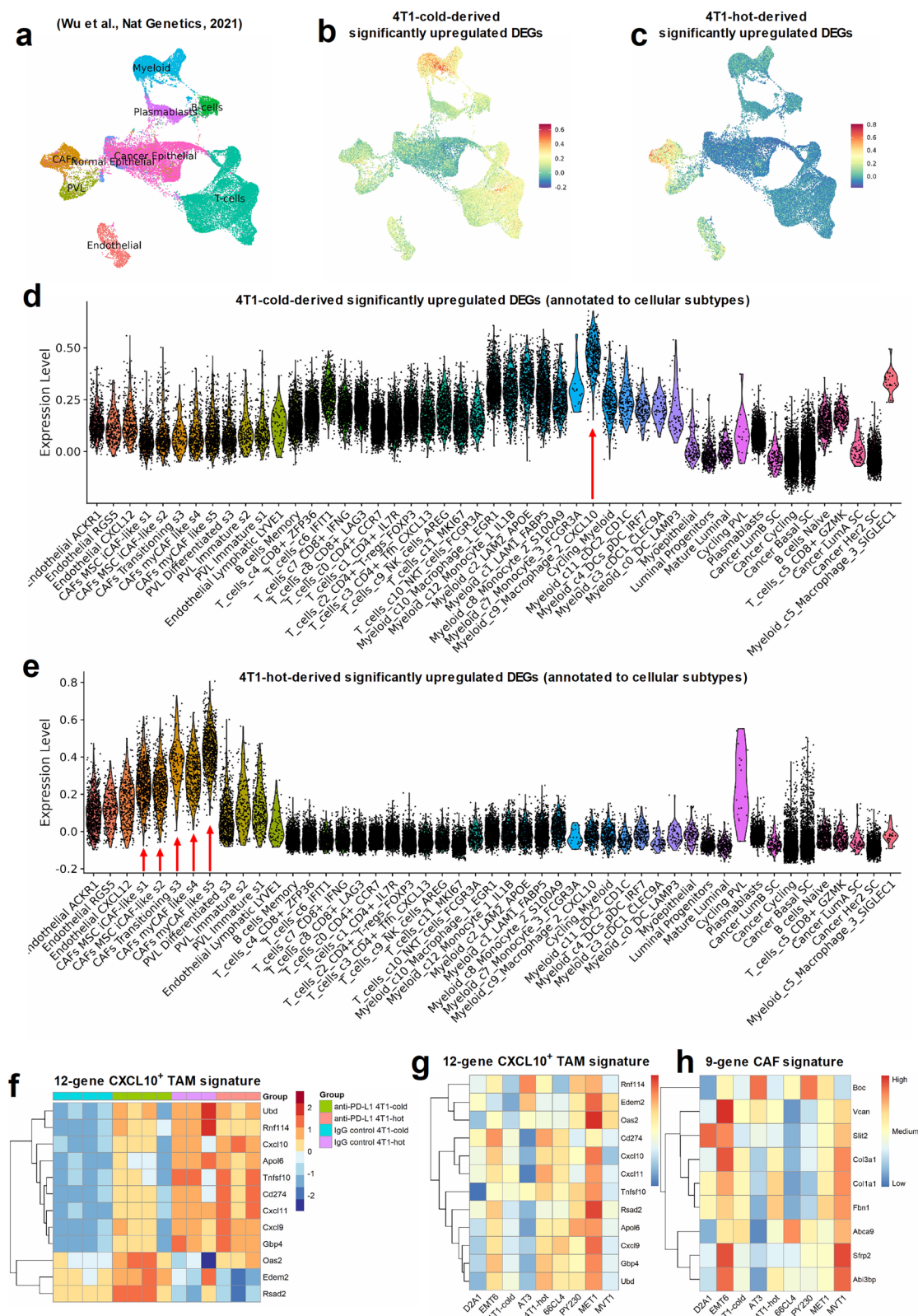
Fig. 6 | Mapping upregulated gene sets in anti-PD-L1-treated 4T1-cold and 4T1-hot primary tumors to respectively CXCL10+ TAMs and CAFs. Significantly upregulated DEGs (based on adjusted *p*-value < 0.05) upon anti-PD-L1 vs IgG control treatment in both 4T1-cold and 4T1-hot primary tumors were mapped to an existing scRNA-seq atlas of human TNBC[25]. **a** UMAP visualization of 42136 cells from 10 TNBC patient tumors. **b, c** UMAP of calculated gene set expression of significantly upregulated DEGs in 4T1-cold (**b**) and 4T1-hot primary tumors (**c**) upon anti-PD-L1 treatment across all clusters. **d, e** Violin plots showing distribution of significantly upregulated DEGs in 4T1-cold (**d**) and 4T1-hot primary tumors (**e**) upon anti-PD-L1 treatment across specific cellular subtype clusters. **f** Heatmaps showing row-normalized expression levels of a 12-gene CXCL10+ TAM signature in 4T1-cold and 4T1-hot primary tumors upon anti-PD-L1 and IgG control treatment. **g, h** Heatmaps showing row-normalized expression levels of a 12-gene CXCL10+ TAM signature (**g**) and a 9-gene CAF signature (**h**) in 9 mouse TNBC cell line-derived primary tumors at an early timepoint (i.e., 2 w.p.i., at 20–30 mm³ primary tumor size).

reactions due to their MYC and VEGF overexpression, driving their systemic progression[11]. Compared to the 4T1-cold counterparts, and in line with their slower growth, 4T1-hot primary tumors showed high expression of gene signatures associated with IFN signaling, T-cell activation, and exhaustion, already at an early timepoint. The transcriptomic data were corroborated by enhanced leukocyte reactions, reflected by increased splenomegaly, with on the one hand significantly increased numbers of dendritic cells (DCs), activated/exhausted T-cells and a higher M1/M2 TAM ratio, and on the other hand a significantly decreased number of T-regs in the 4T1-hot compared to 4T1-cold TIME. Similar to the 4T1-hot TIME, 66CL4 primary tumors comprised a high T-cell and NK cell number, potentially hindering their efficient and fast local progression. Despite their 'hot' TIME, 66CL4 primary tumors are also highly immunosuppressed due to excessive influx of M2 TAMs and additional, albeit limited, infiltration of TANs and PMN-MDSCs in the tumor core.

The similar CD8+ T-cell proliferation in the models, based on Ki67 positivity in the CD8α+ T-cell population, was a striking observation. These data indicate that CD8+ T-cell proliferation in primary tumors is influenced by other factors besides immunosuppressive myeloid cells. For example, the hypoxic TIME with altered metabolism can also strongly impact CD8+ T-cells. Indeed, as identified through our bulk RNA-seq data, all models show reduced fatty acid metabolism and oxidative phosphorylation in their primary tumors, both known to be important for the self-renewal of T-cells[40,41]. Moreover, the increase of glycolysis (i.e., Warburg effect under hypoxic conditions) by tumor cells in all models makes glucose a scarce energy source for T-cell proliferation in the TIME[42]. Hypoxia further supports differentiation of CD8+ T-cells without affecting their IFN-γ or granzyme B expression[43].

Besides the differential immune cell content, the heterogeneity between the models and associated human relevance was further demonstrated based on the classification of the TIME in 5 previously identified TNBC TIME landscapes[22]. Indeed, our results demonstrate that every TIME subtype observed within the TNBC patient population is captured by the 9 characterized mouse TNBC models, ranging from IM in the 4T1-hot model to M in the D2A1 model, BL and LAR in the MET1 and PY230 model, and MSL in the MVT1 model.

Based on their similar strain background, differential 'cold' vs 'hot' TIME, high PD-L1 expression, and resistance to anti-PD-L1, the 4T1-cold- and 4T1-hot-based model were selected to comparatively identify 'cold' and 'hot' TIME adaptation mechanisms to ICB. In preliminary experiments, administration of a second dose of a rat-derived anti–PD-L1 antibody proved lethal. To reduce the risk of toxicity, we subsequently employed a murinized anti–PD-L1 antibody and observed that a second dose was not fatal, suggesting improved tolerability. Although a more frequent dosing regimen might influence tumor growth, particularly in the 4T1-hot model, this treatment regimen was not further tested in the current study and can be regarded as a limitation. Mapping the significantly upregulated DEGs following anti-PD-L1 treatment in 4T1-cold and 4T1-hot primary tumors to a publicly accessible scRNA-seq dataset of TNBC patient tumors[25] revealed distinct cell populations that play an important role in anti-PD-L1 resistance. Although our results could have been further strengthened with data from models that respond to anti-PD-L1 blockade, clinical validation through the GeparNuevo trial data also points towards similar ICB adaptation mechanisms in TNBC patients. Notably, the GeparNuevo patient tumor dataset contains a mixture of immune signatures resembling both the 4T1-hot and 4T1-cold TIME states.

In anti-PD-L1-treated 4T1-cold primary tumors, we identified upregulation of TAM subsets that can influence disease burden. As one of the highest PD-L1-expressing immune cells in the TIME, TAMs are polarized to a pro-inflammatory phenotype upon PD-L1 blockade with decreased expression of arginase 1 (Arg1) and an increase in inducible nitric oxide synthase (iNOS), major histocompatibility complex (MHC)II, and CD40 expression[44]. Moreover, Hartley et al. showed that this pro-inflammatory macrophage activation occurs independently of T-cells and can delay tumor growth in preclinical breast cancer models[45]. We also observed a similar pro-

inflammatory macrophage activation in our study, especially in the anti-PD-L1-treated 4T1-cold model, with the increase of CXCL10+ TAMs. Indeed, these TAMs are commonly described as a positive prognostic factor in cancers, given their role in T-cell recruitment through the CXCL9/10-CXCR3 axis[46–48], which shifts the TIME into a 'hot' state. However, Wu et al. have shown the major immunosuppressive capabilities of CXCL10+ TAMs, specifically in the TNBC subtype, through their high PD-L1 expression and location near CD8+ T-cell-rich regions in patient tumors[25]. The CXCL10+ TAM subset has also been characterized in other studies and was additionally reported to suppress T-cells by indoleamine 2,3-dioxygenase-1 (IDO-1)-mediated tryptophan degradation and CXCL9/10/11-mediated recruitment of T-regs[49,50]. We therefore suggest that CXCL10+ TAMs initially induce T-cell recruitment and activation upon anti-PD-L1 treatment, but subsequently cool down the 'hot' TIME through upregulation of their immunosuppressive mechanisms in response to T-cell- and MDSC-derived IFN signaling, eventually inducing ICB resistance. Moreover, as a 12-gene CXCL10+ TAM signature showed increased expression in the bulk RNA-seq data from the majority of our characterized mouse TNBC models, the presence of these TAMs is presumably a common resistance mechanism across multiple TNBC TIME states. Similar to the CXCL10+ TAM subpopulation, an upregulation of specific lipid-associated macrophages (LAMs) was identified in anti-PD-L1-treated 4T1-cold primary tumors based on the significantly upregulated DEGs. LAMs commonly reside in the highly adipose-rich breast tissue and display anti-inflammatory[51] and immunosuppressive features[52] with high PD-L1 and PD-L2 protein expression[25] in response to IFN signaling, also indicating their potential common role in ICB resistance. JAK signaling is mainly responsible for the type 1 IFN and IFN-γ responses in the TIME, and therefore treatment with JAK inhibitors following anti-PD-L1 blockade may prevent the IFN-induced immunosuppressive CXCL10+ TAM and LAM accumulation. This potential benefit of using JAK inhibitors together with ICB has even recently been shown in the context of non-small cell lung cancer[53] and Hodgkin lymphoma[54] preclinical models and patients. Both studies report that the use of ICB followed by JAK inhibition with itacitinib or ruxolitinib inhibits persistent IFN signaling and progressive differentiation of CD8+ T-cells towards an exhausted state[53,54]. Similar results have also been described in preclinical models for prostate and colorectal cancer upon treatment with ICB and subsequent JAK inhibition with ABT-317[55]. Moreover, combining ICB with ruxolitinib in Hodgkin lymphoma resulted in a significantly reduced infiltration of immunosuppressive granulocytes, including neutrophils and PMN-MDSCS, MHCII upregulation, as well as reduced CXCL10+ TAM and LAM gene signature expression in myeloid cells[54].

In anti-PD-L1-treated 4T1-hot primary tumors, we also identified upregulation of CAFs as a possible ICB resistance mechanism. CAFs are known to play a role in tumor proliferation, angiogenesis, EMT, and pro-tumorigenic TGF-β-signaling[56], which were all upregulated in 4T1-hot primary tumors upon anti-PD-L1 treatment based on cancer hallmark gene signatures. Especially, the myCAF population was upregulated, which is reported to be enriched in invasive cancer regions to generate a stiff TIME and is associated with ICB resistance[25,57]. The iCAFs, which are spatially scattered across the TIME[25], can also transition to myCAFs through a TGF-β gradient established by the tumor and immune cells[58]. In line with this described negative impact of (my)CAF upregulation, high expression of our identified 9-gene CAF signature is also associated with decreased survival in TNBC patients. Given the downregulation of (my)CAF-associated genes in anti-PD-L1-treated 4T1-cold primary tumors, this CAF-induced ICB adaptation is likely less important in the 4T1-cold-based model. However, it could also be of relevance in the MVT1 and EMT6 primary tumors, as their 'cold' TIME displayed an even higher expression of the 9-gene CAF signature compared to the 4T1-hot TIME. Our data further highlight CAF-derived factors, such as versican (VCAN), that could be targeted to alleviate ICB responses in the TNBC TIME. The large chondroitin sulfate proteoglycan VCAN is known for its association with poor ICB efficacy[59] and is highly upregulated in both the anti-PD-L1-adapted 4T1-hot TIME and Durvalumab-treated TNBC patients in the GeparNuevo trial. More

specifically, VCAN supports immunosuppressive CAF-breast cancer cell interactions[60] and creates a physical barrier through binding with hyaluronic acid in the ECM, thereby hindering T-cell infiltration in the TIME[61]. Preventing the VCAN-hyaluronan binding through antibody blockade[62] or proteolytic cleavage of the chondroitin sulfate chains across the VCAN backbone[61] can restore T-cell trafficking and establish an ICB-responsive TIME. Our transcriptomic profiling of anti-PD-L1-treated 4T1-hot primary tumors also pointed towards a potential role of mast cells in ICB efficacy. More specifically, 5 of the 13 most significantly downregulated DEGs in these anti-PD-L1-resistant primary tumors were attributed to mast cells. In line with this hypothesis, a very recent study has shown that mast cell activation is necessary for lymphocyte infiltration and anti-PD-L1 efficacy in human TNBC patients[63]. Although the downregulated mast cell genes in anti-PD-L1-treated 4T1-hot primary tumors could not be annotated to mast cells in the Wu et al. scRNA-seq dataset due to their underrepresentation[25], many other significantly downregulated DEGs were annotated to myoepithelial cells. This highlights a potential loss of myoepithelial barrier cells that normally hinder progressive disease[64], and was also similarly observed in Durvalumab-treated TNBC patients enrolled in the GeparNuevo trial. Alternative to these differential ICB adaptation mechanisms, the high content of immunosuppressive PMN-MDSCs and TANs could also inhibit effective anti-PD-L1 responses in both the 4T1-cold and 4T1-hot model[65]. To this end, our group previously showed that blocking the PMN-MDSC/TAN-associated protein CHI3L1 significantly reduces immunosuppressive myeloid cells in the 4T1-hot-based model and alleviates its resistance to anti-PD-1[19].

In conclusion, our characterized mouse TNBC models and identified anti-PD-L1 adaptation mechanisms now warrant exploration of potential therapeutic targets that hinder ICB adaptation for improved patient outcomes. As our data also point towards the accumulation of CXCL10⁺ TAMs and CAFs as common ICB adaptation mechanisms across TIME states, the identified therapeutic targets for inhibiting the CXCL10⁺ TAM subtype and CAFs could even be relevant to increase ICB efficacy in both 'hot' and 'cold' TIME-associated TNBC patients. Following validation of target inhibition in selected models, clinical translation can subsequently be foreseen through clinical trials.

Methods
Cell culture
4T1-hot cells, commercially available from Sibtech, were provided as a kind gift by Prof. Clare Isacke (Breakthrough Breast Cancer Research Centre, London, UK) and previously used by her research group[66]. These cells constitutively express firefly luciferase and develop a 'hot'/inflammatory TIME in vivo due to the T-cell response against luciferase[67]. Moreover, the cell line has the advantage over other luciferase-expressing 4T1 cell lines (such as the 4T1-luc2 cell line from the American Type Culture Collection (ATCC)) in that it more stably develops progressive primary tumors. EMT6, D2A1, MET1 and MVT1 mammary tumor cells were provided as a kind gift by Dr. Lalage Wakefield (National Cancer Institute, Bethesda, USA)[11]. 4T1-cold and PY230 mammary tumor cells were purchased from ATCC. In contrast to the 4T1-hot cells, the (parental) 4T1-cold cells do not express firefly luciferase and develop a 'colder'/T-cell-deprived TIME in vivo due to the absence of luciferase immunogenicity[67,68]. AT3 mammary tumor cells were purchased from Sigma-Aldrich (Overijse, Belgium). 66CL4 cells were provided as a kind gift by Prof. Traci R. Lyons (University of Colorado Anschutz Medical Campus, Denver, CO, USA). Cell lines were maintained at 37°C and 5% CO₂. The 4T1-hot, 4T1-cold, EMT6, D2A1, MET1 and MVT1 cells were cultured in Dulbecco's Modified Eagle's Medium (DMEM, Thermo Fisher Scientific, Waltham, MA, USA) supplemented with 10% heat-inactivated fetal bovine serum (FBS, Thermo Fisher Scientific) and 100 U/ml penicillin, 100 µg/ml streptomycin (both from Sigma-Aldrich). The 66CL4 cell culture was additionally supplemented with 1% Gibco™ MEM Non-Essential Amino Acids Solution (Thermo Fisher Scientific). AT3 cells were cultured in DMEM (Thermo Fisher Scientific) supplemented with 10% FBS (Sigma-Aldrich), 2 mM Non-Essential Amino Acids Solution and 15 mM HEPES (both from

Thermo Fisher Scientific), 1× EmbryoMax® 2-Mercaptoethanol (Sigma-Aldrich), 100 U/ml penicillin and 100 µg/ml streptomycin (both from Sigma-Aldrich). PY230 cells were cultured in Ham's F-12K (Kaighn's) Medium (Thermo Fisher Scientific) supplemented with 0.1% MITO+ Serum Extender (Corning, Bedford, MA, USA), 5% heat-inactivated FBS, 100 U/ml penicillin and 100 µg/ml streptomycin (all from Thermo Fisher Scientific). All cell lines were routinely checked for mycoplasma and other bacterial contamination using a PlasmoTest™ mycoplasma detection kit (Invivogen, San Diego, USA). Harvesting of confluent cells was performed through incubation with 0.25% trypsin-ethylenediaminetetraacetic acid (EDTA) (Sigma-Aldrich) for 5 min. Cells were centrifuged at 400×g for 5 min for subsequent counting with a Bürker chamber.

In vitro live cell imaging
Cells were seeded at a density of 50,000 cells/well in a 24-well plate in 1 ml of their corresponding phenol red-free medium. The 24-well plate was incubated at 37 °C and 5% CO₂ in the BioTek BioSpa (Agilent, Santa Clara, CA, USA). At 4 h after seeding, the first picture for confluency measurement was taken by the BioTek Cytation 5 (Agilent, Santa Clara, CA, USA) with subsequent measurements every 2 h until a total time of 52 h was reached. Pictures were taken at the center of the well using the montage setting (2 × 2) using 4× magnification in Bright Field: High Contrast channel. Gen5 (version 3.13) software was used to stitch montage pictures together, determine the total picture area, and set thresholds to identify object area (cells) compared to the background. Confluency for every timepoint was determined by calculating (object area/total picture area) × 100. The slope of growth was determined using linear regression on the confluence curve during the log-phase of growth (timepoint before the curve reached the plateau). A total of 3 replicate plates were analyzed. Cells were also seeded at a density of $1 × 10^6$ in T75 flasks and allowed to grow for 48 h in order to determine cell numbers.

Single-cell RNA-sequencing and data processing of cell lines
A total of $2 × 10^6$ cells from each mouse tumor cell line were incubated for 30 min at 4 °C with a unique TotalSeq-A cell hashing antibody specific against mouse CD45 and MHC class I (1:250 diluted, HTO; TotalSeq-A0301 − TotalSeq-A0309 (BioLegend, CA, USA)). After incubation, cells were washed and centrifuged at 400×g, 5 min, 4 °C. The supernatant was discarded, and the cell pellet was subsequently resuspended in 100 µl cell multiplexing oligonucleotides (CMOs) and incubated at room temperature (RT) for 5 min (CMO01–CMO09 (10× Genomics, Pleasanton, CA, USA)). Samples were washed again and resuspended in phosphate buffered saline (PBS) supplemented with 1% bovine serum albumin (BSA) for sorting. DAPI was added to sort out live cells using a BD FACSAria II cell sorter (BD Biosciences, Aalst, Belgium). The tagged sorted cells were pooled (pool 1: D2A1 + MVT1 + EMT6 + MET1 + 4T1-hot; pool 2: 4T1-cold + 66CL4 + AT3 + PY230) and loaded on a Chromium GemCode Single Cell Instrument (10× Genomics) to generate single cell Gel beads-in-EMulsion (GEM). The single cell (sc)RNA-seq libraries were prepared using the GemCode Single Cell 3′ Gel Bead and Library kit, version Next GEM v3.1, according to the manufacturer's instructions (10× Genomics, User Guide CG000388) with the addition of the amplification primer 5'-GTGACTG-GAGTTCAGACGTGTGCTCTTCCGAT*C*T-3′ (3 nM) during cDNA amplification to enrich the TotalSeq-A hashing protein oligos. Size selection with SPRIselect Reagent Kit (B23318, Beckman Coulter, Inc., California, USA) was used to separate amplified cDNA molecules for 3′ gene expression, hashing protein, and hashing lipid construction. TotalSeq-A protein library construction, including sample index PCR using Illumina's TruSeq Small RNA primer sets, and SPRIselect size selection, was performed according to the manufacturer's instructions. The cDNA content of pre-fragmentation and post-sample index PCR samples was analyzed using the 5200 Fragment Analyzer (Agilent). Sequencing libraries were loaded on an Illumina NovaSeq flow cell with sequencing settings according to the recommendations of 10× Genomics. The Cell Ranger pipeline (10× Genomics, version 7.1.0) was used to perform sample demultiplexing and to generate FASTQ files for read 1, read 2, and the i5, i7 sample index for the gene expression, HTO, and CMO

libraries. Read 2 of the gene expression libraries was mapped to the reference genome (mouse mm10-2020-A). Subsequent barcode processing, unique molecular identifiers filtering, and gene counting were performed using the Cell Ranger suite (10× Genomics). Data analysis was performed using Seurat (version 4.1.3). The conversion from the raw feature matrix (raw_feature_bc_mattrix.h5) to the Seurat object applied a filtering of each cell containing at least 200 genes and each of the genes being expressed in at least three cells. The metadata column "cellranger_demultiplexing" was created based on the information from assignment_confidence_table.csv created by CellRanger. Extra demultiplexing was done, using the algorithms HTODemux and MULTIseqDemux (Seurat), on both the HTO and CMO data. Before demultiplexing, the data were filtered to only retain the features used to hash the subsamples. Cells were filtered based on nmads, 5 nmads were used as a cutoff for high/low number of genes and number of UMIs, and 25 nmads for the percentage of mitochondrial genes. After filtering, the standard Seurat pipeline was used to process the data. Seurat objects were merged together using the merge() function. Singlet cells were selected based on "CMO_H-TODemux_classification.global". The standard Seurat pipeline was performed on the merged Seurat object. The FindNeighbors() function was used to calculate nearest neighbors for each cell using the first 25 principal components (PCs). Cell clusters were identified based on a shared nearest neighbor (SNN) with a 0.1 resolution. According to the CMO label, clusters were annotated as their respective cell line.

Expression of cytokines and chemokines was checked based on gene lists from the NanoString Mouse PanCancer Immune Profiling. The FindAllMarkers() function was used with 0.2 thresholds for both log-fold change and minimum difference in percentage to identify differential expression for each cell line. Area under the curve (AUC) value was calculated for all genes using the wilcoxaux() function, and genes were ranked according to their AUC value. Gene set enrichment analysis (GSEA) was performed on the ranked list of genes using the fgsea package in R for the Mus musculus hallmark collection (Broad Institute), with p-adjusted < 0.05 considered as significant.

Human single-cell analyses from a publicly available scRNA-seq dataset

For human single-cell analyses, publicly available pre-processed data and cell annotation of breast tumor samples as published by Wu et al.[25] were downloaded from the Human Cell Atlas (singlecell.broadinstitute.org), and only tumor samples from TNBC patients were retained. Human orthologs of the significantly up- and downregulated differentially expressed mouse genes from the anti-PD-L1 adaptation experiment were identified using the Ensemble BioMart database. Single-cell gene set expression of these genes was calculated using the Seurat AddModuleScore() function. Canonical markers and signature-based annotation using Garnett were used to annotate clusters to their cell types according to the Wu et al. publication[25]. A similar approach was used to map the significantly up- and downregulated differentially expressed genes in the Durvalumab arm from the GeparNuevo trial dataset to specific cell subsets. Both human datasets were generated following approval of the relevant institutional ethics committees (Wu et al.[25]: Sydney Local Health District Ethics Committee, Royal Prince Alfred Hospital zone, and the St Vincent's hospital Ethics Committee (x13-0133, x19-0496, x16-018, and x17-155); Denkert et al.[26]: ethics committee of the Philipps University Marburg (38/20 and 121/20)) and with written consent of all patients involved.

Intraductal inoculation and antibody treatment

Animal experiment protocols were approved by the Ethical Committee (EC) of the Faculty of Veterinary Medicine, Ghent University (EC 2023-011, EC 2023-087, and EC 2024-032) and performed according to Good Scientific Practice principles. Female mice of 8-weeks-old were mated with male mice of the same strain and gave birth to pups within 3 weeks. Pups were weaned 12–14 days later, after which lactating mother mice were intraductally inoculated in the third mammary gland pair with 5×10^4 D2A1, 5×10^4 EMT6, 4×10^3 4T1-cold, 2×10^5 AT3, 5×10^4 4T1-hot, 2×10^5 66CL4, 2×10^5 PY230, 12.5×10^3 MET1 or 12.5×10^3 MVT1 cells suspended in a cold

mixture of PBS and Matrigel® (1:10; Corning) under isoflurane inhalation and buprenorphine analgesia. This mammary intraductal (MIND) approach introduces mammary tumor cells within the natural microenvironment of the mammary ducts, providing a relevant platform that recapitulates the initiation and progression of TNBC and spontaneous metastasis in immunocompetent mice[69]. Moreover, the use of lactating instead of virgin female mice provides a more accessible mammary teat canal for a 32 G pediatric needle and does not necessitate microscopic guidance or surgery, which can be influential on the TIME and animal welfare.

For the anti-PD-L1 adaptation experiment, 4T1-based models were assigned to a group and treated, single-blinded. Recombinant anti-mPD-L1-mIgG1 clone B7-H1 (BioXCell, West Lebanon, NH, USA) or isotype control mouse IgG1 clone MOPC-21 (BioXCell) was weekly systemically administered through intraperitoneal (i.p.) injection at 200 µg/mouse.

At the end of the experiments, mice were sedated with a ketamine (100 mg/kg, Ketamidor, Ecuphar nv/sa, Oostkamp, Belgium) and xylazine (10 mg/kg, xylazini hydrochloridum, Val d'Hony-Verdifarm, Beringen, Belgium) mixture and sacrificed through cervical dislocation. Primary tumors, spleen and lungs were isolated for further analysis.

Bulk RNA-sequencing and data processing of primary tumors

RNA was extracted from primary tumors of all models at 2 w.p.i. and from healthy mammary glands of Matrigel®-inoculated BALB/C, C57BL/6, and FVB/N mice ($n = 3$ for all primary tumors and healthy mammary glands, except n = 4 for PY230 and AT3 primary tumors) using the RNeasy Mini Kit (Qiagen, Valencia, CA, USA) according to the manufacturer's instructions. RNA was extracted from IgG control- and anti-PD-L1-treated 4T1-cold and 4T1-hot primary tumors at 3 w.p.i. ($n = 4$ for both 4T1-cold groups and $n = 3$ for both 4T1-hot groups) using the same kit. For the anti-PD-L1-treated tumors, samples were harvested 7 days after the first antibody dose, immediately prior to the second dose, in order to mirror sample collection strategies in human clinical trials such as SYNERGY[70] (adjuvant anti-PD-L1 combined with chemotherapy in previously untreated locally advanced or metastatic TNBC patients) and GeparNuevo[26] (neoadjuvant anti-PD-L1 in non-metastatic TNBC), which collected biopsies after a single ICB dose to investigate early transcriptomic changes. Extracted RNA was stored at $-80\,°C$ until downstream transcriptomic analysis using Illumina's TruSeq chemistry in collaboration with Azenta Life Sciences (Leipzig, Germany). A total amount of 250 ng RNA was converted into sequencing libraries, and sequencing (2×150 bp) was performed on a NovaSeq instrument (Illumina Inc., San Diego, CA, USA), aiming for 10 M reads per sample. Raw reads were mapped to the murine reference genome (version mm10) using HISTAT2, and the resulting SAM files were converted to sorted BAM files using *samtools*. The number of mapped reads per genomic location was counted using the summariseOverlaps function from the BioC-package *GenomicAlignments* in the intersection non-empty mode, taking strand information and unpaired reads into account. All genes with raw expression counts above ten in at least 20% of the cases were filtered for further analysis. Raw count data were normalized using variance stabilizing normalization and analyzed for differential expression using the DESeq2 package in BioConductor.

Differential expression of 2-week primary tumors was obtained for each model in comparison to their respective healthy control mammary gland, excluding the mouse strain-dependent transcriptomic/inflammatory differences. These calculated log2-fold changes in expressed genes from each model were presented in a heatmap using the pheatmap package with selection of different gene sets from the NanoString Mouse Immune Exhaustion Gene List, Mouse Myeloid Innate Immunity V2, and Mouse Tumor Signaling 360 panels. DESeq2 results of differentially expressed genes for each model were ranked based on log2-fold change and p-value (log2FC×(-log10(pvalue))). Hallmarks of cancer were determined using the fgsea package for the Mus musculus hallmark collection (Broad Institute) and using a ranked list of genes for each model with thresholds for min-Size = 10 and maxSize = 500.

For TNBC TIME classification, mouse genes were mapped onto their respective human orthologs (R library orthogene 1.8.0), retaining 85% of all

genes (14,213 genes) in our gene expression matrix. TNBC subtypes were then computed as previously described by Garcia et al. by applying the TNBCclassif function (https://github.com/BCTL-Bordet/TNBC_molecularsubtypes/tree/main) on VST-normalized counts[71]. The obtained coefficients from the classifier were visualized using the R library ComplexHeatmap 2.18.0.

Volcano plots comparing the 2-week 4T1-cold vs 4T1-hot primary tumors or anti-PD-L1 vs IgG control-treated primary tumors were generated based on DESeq2 results, identifying upregulated genes based on log2-fold change > 0.5 and adjusted p-value < 0.05, and downregulated genes based on log2-fold change < -0.5 and adjusted p-value < 0.05.

Histology and immunohistochemistry
Primary tumor, lung and spleen tissue were fixed in 3.5% phosphate-buffered formaldehyde for 24 h, then transferred to 70% ethanol and subsequently paraffin-embedded. For histology, 5 μm sections were deparaffinized, rehydrated and stained with H&E. For immunohistochemical stainings, 2–3 μm sections were deparaffinized, rehydrated and subjected to pressurized antigen retrieval for 30 min at 95 °C using a 10 mM citrate buffer (VWR International, Leuven, Belgium) at pH 6 (for Ly6G, CD163 and CD8α) or a 10 mM Tris-1 mM EDTA buffer (Sigma-Aldrich) at pH 9 (for cytokeratin 5), supplemented with 0.05% Tween 20 (Sigma-Aldrich). Endogenous peroxidase was blocked using 3% H_2O_2 (Sigma-Aldrich) in methanol for 10 min, and non-specific protein binding was blocked using serum-free protein blocking buffer (Dako, Heverlee, Belgium) for 10 min. Primary antibodies were diluted in antibody diluent (Dako) and incubated for 1 h at RT: cytokeratin 5 (host: rabbit, clone: EP1601Y, dilution: 1/100), Ly6G (host: rat, clone: 1A8, dilution: 1/1000), CD163 (host: rabbit, clone: EPR19518, dilution: 1/500) and CD8α (host: rabbit, clone: EPR21769, dilution: 1/2000). Either Rat-on-Mouse HRP-Polymer (Biocare Medical, CA, USA) or Dako EnVision + Rabbit (Dako) was used as a secondary antibody for 30 min at RT. Slides were kept in a humidified box throughout the procedure and washed 3 × 5 min with tris-buffered saline (TBS, Thermo Fisher Scientific) between every incubation step. The slides were treated for 10 min with a 3,3'-diaminobenzidine (DAB)-containing buffer (Dako) to detect positive staining, counterstained for 5 min in Harris Hematoxylin (Carl Roth, Karlsruhe, Germany) and 1 min in 0.1 N HCl (Sigma-Aldrich), dehydrated, and mounted with Entellan (Sigma-Aldrich). The complete tissue slide was scanned (20× magnification) using a brightfield digital slide scanner PANNORAMIC 250 Flash III (3DHistech, Budapest, Hungary) and analyzed using QuPath. Stain vectors were estimated and adjusted to represent the DAB en H signal. Using combined colors, a thresholder was created to classify pixels for tumor tissue and DAB signal. Artefacts were removed using the wand tool in QuPath. Staining positivity was calculated as a percentage of the total tumor area ((DAB area)/total tumor area) × 100).

Flow cytometric immunophenotyping
Primary tumors were isolated upon scarification and digested into single cell suspensions using a commercially available tumor dissociation enzyme kit and gentleMACS Dissociator with accompanying C tubes (Miltenyi Biotec, Leiden, The Netherlands) as previously described[21].

The number of cells was determined by adding 20 μl of TruCount beads (BD Biosciences) to 180 μl of diluted cell suspension and analyzing on a CytoFLEX flow cytometer (Beckman Coulter). Absolute numbers of cells were calculated with Trucount technology, taking the dilution factor into account. Cellular viability was evaluated by viobility 488/520 fixable dye staining (Miltenyi Biotec) according to the manufacturer's instructions. Cellular stainings were performed as previously described[19,21]. Used fluorophore-conjugated antibodies and concentrations for cellular stainings were previously described[19,21]. Following immune cell populations were selected to be analyzed: CD45+ CD11b+ CD14+ Ly6Cint Ly6G+ PMN-MDSCs, CD45+ CD11b+ CD14+ Ly6Chi Ly6G− M-MDSCs, CD45+ CD11b+ CD14− Ly6Cint Ly6G+ TANs, CD45+ CD11b+ CD14+ F4/80+ TAMs, and also more specific CD45+ CD11b+ CD14+ F4/80+ CD80+ MHCII+ M1 TAM and CD45+ CD11b+ CD14+ F4/80+ CD206+ M2 TAM

subtypes, CD45+ CD11b+ F4/80- CD11c+ MHCII+ DCs, CD4+ and CD8α+ T-cells (CD45+ CD3ε + CD4+ CD8α− and CD45+ CD3ε+ CD4− CD8α+, respectively), CD45+ CD3ε− NKp46− CD19+ B220+ B-cells, CD45+ CD3ε− NKp46+ NK and CD45+ CD3ε+ NKp46+ NK-T cells. Gating strategy was applied as previously described[19]. Applying CD14 to discriminate between TANs and immunosuppressive PMN-MDSCs was based on a previous report[72].

Cytokine and immune checkpoint profiling
Whole tumor lysate preparation and subsequent protein concentration determination were performed as previously described[73]. G-CSF, IFN-γ, MIP-2, and PD-L1 were investigated in 50 μg of the prepared lysates using the Luminex Multiplex Assay (ProcartaPlex, Thermo Fisher Scientific).

Statistical analysis
Differences between groups were calculated by unpaired Student's t-test or analysis of variance (ANOVA) tests, followed by Newman-Keuls post-hoc testing. p-values < 0.05 were identified as statistically significant. When necessary, data were normalized through $\log_{10}$ transformation. Statistics and data normalization were performed with Prism (Graphpad).

Data availability
The murine RNA-sequencing data generated in this study are publicly available in Gene Expression Omnibus (GEO). Processed and raw scRNA-seq data from mouse TNBC cell lines are available under accession number GSE291126, bulk RNA-seq data from mouse primary tumors at 2 w.p.i. are available under accession number GSE292146, and bulk RNA-seq data from IgG control- and anti-PD-L1-treated 4T1-based models are available under accession number GSE290815. Processed TNBC patient tumor-derived scRNA-seq expression data analyzed in this study were obtained from GEO at GSE176078. GeparNuevo trial bulk RNA-seq expression data were obtained from GitHub (https://github.com/tkarn/G9-HTG). Other datasets generated and/or analyzed during the current study are available from the corresponding author on reasonable request.

Code availability
All used R packages and associated code are available in BioConductor, open source software for bioinformatics, or GitHub, with the link provided in the methods section.

References
1. Ribeiro, R., Carvalho, M. J., Goncalves, J. & Moreira, J. N. Immunotherapy in triple-negative breast cancer: Insights into tumor immune landscape and therapeutic opportunities. *Front. Mol. Biosci.* **9**, 903065 (2022).
2. Thomas, R., Al-Khadairi, G. & Decock, J. Immune checkpoint inhibitors in triple negative breast cancer treatment: promising future prospects. *Front. Oncol.* **10**, 600573 (2021).
3. Parvez, A. et al. PD-1 and PD-L1: architects of immune symphony and immunotherapy breakthroughs in cancer treatment. *Front. Immunol*. **14**, 1296341 (2023).
4. Schmid, P. et al. Pembrolizumab for early triple-negative breast cancer. *N. Engl. J. Med.* **382**, 810–821 (2020).
5. Galon, J. & Bruni, D. Approaches to treat immune hot, altered and cold tumours with combination immunotherapies. *Nat. Rev. Drug Discov.* **18**, 197–218 (2019).
6. Yang, Y., Li, H., Yang, W. & Shi, Y. Improving efficacy of TNBC immunotherapy: based on analysis and subtyping of immune microenvironment. *Front Immunol.* **15**, 1441667 (2024).
7. Xiao, Y. et al. Multi-omics profiling reveals distinct microenvironment characterization and suggests immune escape mechanisms of triple-negative breast cancer. *Clin. Cancer Res.* **25**, 5002–5014 (2019).

8. Tofigh, A. et al. The prognostic ease and difficulty of invasive breast carcinoma. *Cell Rep.* **9**, 129–142 (2014).

9. Yin, L., Duan, J. J., Bian, X. W. & Yu, S. C. Triple-negative breast cancer molecular subtyping and treatment progress. *Breast Cancer Res.* **22**, 1–13 (2020).

10. Steenbrugge, J. et al. Comparison of the adipose and luminal mammary gland compartment as orthotopic inoculation sites in a 4T1-based immunocompetent preclinical model for triple-negative breast cancer. *J. Mammary Gland Biol. Neoplasia* **21**, 113–122 (2016).

11. Yang, Y. et al. Immunocompetent mouse allograft models for development of therapies to target breast cancer metastasis. *Oncotarget* **8**, 30621–30643 (2017).

12. Khan, K. A. et al. Immunostimulatory and anti-tumor metronomic cyclophosphamide regimens assessed in primary orthotopic and metastatic murine breast cancer. *npj Breast Cancer* **6**, 29 (2020).

13. Falvo, P. et al. Cyclophosphamide and vinorelbine activate stem-like CD8þ T cells and improve anti-PD-1 efficacy in triple-negative breast cancer. *Cancer Res.* **81**, 685–697 (2021).

14. Xia, L. et al. Targeting triple-negative breast cancer with combination therapy of EGFR CAR T cells and CDK7 inhibition. Cancer. *Immunol. Res.* **9**, 707–722 (2021).

15. Katuwal, N. B. et al. Preclinical platform using a triple-negative breast cancer syngeneic murine model to evaluate immune checkpoint inhibitors. *Anticancer Res.* **43**, 85–95 (2023).

16. Krockenberger, M. et al. Macrophage migration inhibitory factor contributes to the immune escape of ovarian cancer by down-regulating NKG2D. *J. Immunol.* **180**, 7338–7348 (2008).

17. Klement, J. D. et al. An osteopontin/CD44 immune checkpoint controls CD8 + T cell activation and tumor immune evasion. *J. Clin. Invest.* **128**, 5549–5560 (2018).

18. Dowling, R. J. O. et al. mTORCl-mediated cell proliferation, but not cell growth, controlled by the 4E-BPs. *Science* **328**, 1172–6 (2010).

19. Salembier, R. et al. Chitin-mediated blockade of chitinase-like proteins reduces tumor immunosuppression, inhibits lymphatic metastasis and enhances anti-PD-1 efficacy in complementary TNBC models. *Breast Cancer Res.* **26**, 63 (2024).

20. DuPre', S. A. & Hunter, K. W. Jr. Murine mammary carcinoma 4T1 induces a leukemoid reaction with splenomegaly: association with tumor-derived growth factors. *Exp. Mol. Pathol.* **82**, 12–24 (2007).

21. Steenbrugge, J. et al. One cisplatin dose provides durable stimulation of anti-tumor immunity and alleviates anti-PD-1 resistance in an intraductal model for triple-negative breast cancer. *Oncoimmunology* **11**, 2103277 (2022).

22. Wang, X. et al. Spatial transcriptomics reveals substantial heterogeneity in triple-negative breast cancer with potential clinical implications. *Nat. Commun.* **15**, 1–22 (2024).

23. Mall, C. et al. Repeated PD-1/PD-L1 monoclonal antibody administration induces fatal xenogeneic hypersensitivity reactions in a murine model of breast cancer. *Oncoimmunology* 5, **e1075114** (2015).

24. Monjazeb, A. M. et al. Mouse preclinical cancer immunotherapy modeling involving anti-PD-1 therapies reveals the need to use mouse reagents to mirror clinical paradigms. *Cancers* **13**, 1–13 (2021).

25. Wu, S. Z. et al. A single-cell and spatially resolved atlas of human breast cancers. *Nat. Genet.* **53**, 1334–1347 (2021).

26. Denkert, C. et al. Molecular adaptation to neoadjuvant immunotherapy in triple-negative breast cancer. *Cell Rep. Med.* **5**, 101825 (2024).

27. Yu, J. W. et al. Tumor-immune profiling of murine syngeneic tumor models as a framework to guide mechanistic studies and predict therapy response in distinct tumor microenvironments. *PLoS One* **13**, e0206223 (2018).

28. Swierczak, A. et al. The promotion of breast cancer metastasis caused by inhibition of CSF-1R/CSF-1 signaling is blocked by targeting the G-CSF receptor. Cancer. *Immunol. Res.* **2**, 765–776 (2014).

29. Pande, K. et al. Cancer-induced expansion and activation of CD11b +Gr-1+ cells predispose mice to adenoviral-triggered anaphylactoid-type reactions. *Mol. Ther.* **17**, 508–515 (2009).

30. Gambardella, G. et al. A single-cell analysis of breast cancer cell lines to study tumour heterogeneity and drug response. *Nat. Commun.* **13**, 1714 (2022).

31. Dave, A. et al. The breast cancer single-cell atlas: defining cellular heterogeneity within model cell lines and primary tumors to inform disease subtype, stemness, and treatment options. *Cell. Oncol.* **46**, 603–628 (2023).

32. Steenbrugge, J. et al. Comparative profiling of metastatic 4T1- vs. non-metastatic Py230-based mammary tumors in an intraductal model for triple-negative breast cancer. *Front. Immunol.* **10**, 495911 (2019).

33. Yu, L., Chen, X., Sun, X., Wang, L. & Chen, S. The Glycolytic Switch in Tumors: How Many Players Are Involved? *J. Cancer* **8**, 3430–3440 (2017).

34. Lee, J. V. et al. Combinatorial immunotherapies overcome MYC-driven immune evasion in triple negative breast cancer. *Nat. Commun.* **13**, 3671 (2022).

35. Bao, L., Cardiff, R. D., Steinbach, P., Messer, K. S. & Ellies, L. G. Multipotent luminal mammary cancer stem cells model tumor heterogeneity. *Breast Cancer Res.* **17**, 1–14 (2015).

36. Spiegel, A. et al. Neutrophils suppress intraluminal NK cell-mediated tumor cell clearance and enhance extravasation of disseminated carcinoma cells. *Cancer Discov.* **6**, 630–649 (2016).

37. Li, P. et al. Lung mesenchymal cells elicit lipid storage in neutrophils that fuel breast cancer lung metastasis. *Nat. Immunol.* **21**, 1444–1455 (2020).

38. Piranlioglu, R. et al. Primary tumor-induced immunity eradicates disseminated tumor cells in syngeneic mouse model. *Nat. Commun.* **10**, 1430 (2019).

39. Cao, Y. et al. BMP4 inhibits breast cancer metastasis by blocking myeloid-derived suppressor cell activity. *Cancer Res.* **74**, 5091–5102 (2014).

40. Tang, Y., Chen, Z., Zuo, Q. & Kang, Y. Regulation of CD8 + T cells by lipid metabolism in cancer progression. *Cell. Mol. Immunol.* **21**, 1215–1230 (2024).

41. Vardhana, S. A. et al. Impaired mitochondrial oxidative phosphorylation limits the self-renewal of T cells exposed to persistent antigen. *Nat. Immunol.* **21**, 1022–1033 (2020).

42. Heiden, M. G. V., Cantley, L. C. & Thompson, C. B. Understanding the warburg effect: the metabolic requirements of cell proliferation. *Science* **324**, 1029–1033 (2009).

43. Bannoud, N. et al. Hypoxia supports differentiation of terminally exhausted CD8 T cells. *Front Immunol.* **12**, 660944 (2021).

44. Xiong, H. et al. Anti-PD-L1 treatment results in functional remodeling of the macrophage compartment. *Cancer Res.* **79**, 1493–1506 (2019).

45. Hartley, G. P., Chow, L., Ammons, D. T., Wheat, W. H. & Dow, S. W. Programmed cell death ligand 1 (PD-L1) signaling regulates macrophage proliferation and activation. Cancer. *Immunol. Res.* **6**, 1260–1273 (2018).

46. House, I. G. et al. Macrophage-derived CXCL9 and CXCL10 are required for antitumor immune responses following immune checkpoint blockade. *Clin. Cancer Res.* **26**, 487–504 (2020).

47. Wei, C. et al. Tumor-associated macrophage clusters linked to immunotherapy in a pan-cancer census. *npj Precis. Oncol.* **8**, 176 (2024).

48. Ardighieri, L. et al. Infiltration by CXCL10 secreting macrophages is associated with antitumor immunity and response to therapy in ovarian cancer subtypes. *Front Immunol.* **12**, 690201 (2021).

49. Mulder, K. et al. Cross-tissue single-cell landscape of human monocytes and macrophages in health and disease. *Immunity* **54**, 1883–1900.e5 (2021).

50. Ma, R. Y., Black, A. & Qian, B. Z. Macrophage diversity in cancer revisited in the era of single-cell omics. *Trends Immunol.* **43**, 546–563 (2022).

51. Jaitin, D. A. et al. Lipid-associated macrophages control metabolic homeostasis in a Trem2-dependent manner. *Cell* **178**, 686–698.e14 (2019).

52. Timperi, E. et al. Lipid-associated macrophages are induced by cancer-associated fibroblasts and mediate immune suppression in breast cancer. *Cancer Res.* **82**, 3291–3306 (2022).

53. Mathew, D. et al. Combined JAK inhibition and PD-1 immunotherapy for non-small cell lung cancer patients. *Science* **384**, eadf1329 (2024).

54. Zak, J. et al. JAK inhibition enhances checkpoint blockade immunotherapy in patients with Hodgkin lymphoma. *Science* **384**, eade8520 (2024).

55. Arias-Badia, M. et al. Sequential JAK inhibition enhances antitumor immunity after combined anti-PD-1 and anti-CTLA4. *JCI Insight*. **10**, e187921 (2025).

56. Jenkins, L. et al. Cancer-associated fibroblasts suppress CD8 + T-cell infiltration and confer resistance to immune-checkpoint blockade. *Cancer Res* **82**, 2904–2917 (2022).

57. Kieffer, Y. et al. Single-cell analysis reveals fibroblast clusters linked to immunotherapy resistance in cancer. *Cancer Discov.* **10**, 1330–1351 (2020).

58. Papait, A. et al. Fight the cancer, hit the CAF!. *Cancers* **14**, 3570 (2022).

59. Hirani, P., Gauthier, V., Allen, C. E., Wight, T. N. & Pearce, O. M. T. Targeting versican as a potential immunotherapeutic strategy in the treatment of cancer. *Front. Oncol.* **11**, 712807 (2021).

60. Shi, Y. et al. Resveratrol suppresses growth and VCAN expression in a Cancer-associated fibroblast-breast Cancer hybrid organoid. *Int. Immunopharmacol.* **153**, 114451 (2025).

61. Hirani, P. et al. Versican associates with tumor immune phenotype and limits T-cell trafficking via chondroitin sulfate. *Cancer Res. Commun.* **4**, 970–985 (2024).

62. Evanko, S. P., Potter-Perigo, S., Bollyky, P. L., Nepom, G. T. & Wight, T. N. Hyaluronan and versican in the control of human T-lymphocyte adhesion and migration. *Matrix Biol.* **31**, 90–100 (2012).

63. Yuanyuan Zhang, A. et al. Distinct cellular mechanisms underlie chemotherapies and PD-L1 blockade combinations in triple-negative breast cancer. *Cancer Cell* **43**, 446–463.e7 (2025).

64. Barsky, S. H. & Karlin, N. J. Mechanisms of disease: breast tumor pathogenesis and the role of the myoepithelial cell. *Nat. Clin. Pract. Oncol.* **3**, 138–151 (2006).

65. Raskov, H., Orhan, A., Gaggar, S. & Gögenur, I. Neutrophils and polymorphonuclear myeloid-derived suppressor cells: an emerging battleground in cancer therapy. *Oncogenesis* **11**, 22 (2022).

66. Ashenden, M. et al. An in vivo functional screen identifies JNK signaling as a modulator of chemotherapeutic response in breast cancer. *Mol. Cancer Ther.* **16**, 1967–1978 (2017).

67. Baklaushev, V. P. et al. Luciferase expression allows bioluminescence imaging but imposes limitations on the orthotopic mouse (4T1) model of breast cancer. *Sci. Rep.* **7**, 1–17 (2017).

68. Lu, Y. et al. Evaluating the immunologically "cold" tumor microenvironment after treatment with immune checkpoint inhibitors utilizing PET imaging of CD4 + and CD8 + T cells in breast cancer mouse models. *Breast Cancer Res.* **26**, 1–15 (2024).

69. Luo, X. L. et al. Development and characterization of mammary intraductal (MIND) spontaneous metastasis models for triple-negative breast cancer in syngeneic mice. *Sci. Rep.* **10**, 1–11 (2020).

70. Buisseret, L. et al. Paclitaxel plus carboplatin and durvalumab with or without oleclumab for women with previously untreated locally advanced or metastatic triple-negative breast cancer: the randomized SYNERGY phase I/II trial. *Nat. Commun.* **14**, 7018 (2023).

71. Garcia, A. J. et al. Differential benefit of metronomic chemotherapy among triple-negative breast cancer subtypes treated in the IBCSG trial 22–00. *Clin. Cancer Res.* **29**, 4908–4919 (2023).

72. Veglia, F. et al. Analysis of classical neutrophils and polymorphonuclear myeloid-derived suppressor cells in cancer patients and tumor-bearing mice. *J. Exp. Med.* **218**, e20201803 (2021).

73. Steenbrugge, J. et al. OMO-1 reduces progression and enhances cisplatin efficacy in a 4T1-based non-c-MET addicted intraductal mouse model for triple-negative breast cancer. *npj Breast Cancer* **7**, 27 (2021).

Author contributions

J.S. and E.M. conceived and designed the study. R.S., C.D.H., and K.D. acquired the data. R.S., C.D.H., K.D., S.V.L., L.C., N.V.R., and J.S. analyzed and interpreted the data. R.S. drafted the manuscript. C.D.H., K.D., S.V.L., L.C., N.V.R., C.S., E.M., and J.S. critically revised the manuscript. R.S., C.D.H., K.D., S.V.L., L.C., N.V.R., C.S., E.M., and J.S. gave their approval of the final manuscript.

Competing interests

The authors declare no competing interests.

Additional information

Supplementary information The online version contains supplementary material available at https://doi.org/10.1038/s41523-025-00880-2.

Correspondence and requests for materials should be addressed to Jonas Steenbrugge.

Reprints and permissions information is available at http://www.nature.com/reprints

Publisher's note Springer Nature remains neutral with regard to jurisdictional claims in published maps and institutional affiliations.